Aus der Klinik für Kardiologie und Pneumologie

(Prof. Dr. med. G. Hasenfuß)

der Medizinischen Fakultät der Universität Göttingen

Nanodomain clustering mechanisms of Junctophilin-2 in human kidney, cardiac and skeletal muscle cells

INAUGURAL - DISSERTATION

zur Erlangung des Doktorgrades

der Medizinischen Fakultät der

Georg-August-Universität zu Göttingen

vorgelegt von

Maximilian Zandt

aus

Gießen

Göttingen 2019

Dekan:	Prof. Dr. med. W. Brück
Referent:	Prof. Dr. med. Stephan E. Lehnart
Ko-Referent/in:	Prof. Dr. Niels Voigt
Tag der mündlichen Prüfung:	13.10.2020

Hiermit erkläre ich, die Dissertation mit dem Titel ″Nanodomain clustering mechanisms of Junctophilin-2 in human kidney, cardiac and skeletal muscle cells″ eigenständig angefertigt und keine anderen als die von mir angegebenen Quellen verwendet zu haben.

Göttingen, den …… ……

(Unterschrift)

Table of contents

List of figures

List of tables

List of abbreviations

BCS	Bovine Calf Serum
Bin1	Myc Box-Dependent-Interacting Protein 1
Ca^{2+}	Calcium, ionic
Cav1.1	L-Type Calcium Channel, Subunit α_1
Cav1.2	L-Type Calcium Channel, Subunit α_2
Cav3	Caveolin 3
CICR	Calcium Induced Calcium Release
CLSM	Confocal Laser Scanning Microscopy
CRU	Calcium Release Unit
DAPI	4’6-diamidino-2-phenylindole
DMEM	Dulbecco’s Modified Eagle’s Medium
DR	Divergent Region
ECC	Excitation-Contraction Coupling
EM	Electron Microscopy
ER	Endoplasmic Reticulum
FWHM	Full Width at Half Maximum
HCM	Hypertrophic Cardiomyopathy
HEK	Human Embryonic Kidney
HF	Heart Failure
HL-1	Human Promyelocytic Leukaemia Cell 1
IF	Immunofluorescence

I/R	Ischemia Reperfusion
JPH	Junctophilin
jSR	Junctional Sarcoplasmic Reticulum
K^+	Potassium, ionic
LTCC	L-Type Calcium Channel
MORN	Membrane Occupation and Recognition Nexus
Na^+	Sodium, ionic
NCX	Sodium Calcium Exchanger
NND	Nearest Neighbour Distance
NRCM	Neonatal Rat Cardiomyocytes
ORAI1	Calcium Release-Activated Calcium Channel Protein 1
PBS	Phosphate Buffered Saline
PFA	Paraformaldehyde
PI3K	Phosphoinositide-3-Kinase
PM	Plasma Membrane
PSF	Point-Spread-Function
ROI	Region of Interest
RyR	Ryanodine Receptor
SERCA	Sarcoplasmic Endoplasmic Reticulum Calcium ATPase
SL	Sarcolemma
SR	Sarcoplasmic Reticulum
STED	STimulated Emission Depletion
STIM1	Stromal Interaction Molecule 1

dSTORM	Direct STochastic Optical Reconstruction Microscopy
TAC	Transverse Aortic Constriction
TM	Transmembrane
TnC	Troponin C
TRPC3	Transient Receptor Potential Channel 3
TT	Transverse Tubule, T-Tubule
WGA	Wheat Germ Agglutinin

1. Introduction

1.1 Epidemiology and clinical significance of heart failure

Heart failure (HF) is a leading clinical syndrome currently attributed to decreased ventricular filling and/or a reduced systolic function (Yancy et al. 2013). Different primary (i.e., genetic) and acquired (i.e., myocardial infarction) disease forms all lead to HF, which is defined both by structural and functional abnormalities (Yancy et al. 2013).

Several studies emphasise the increasing prevalence of and the associated economic strain caused by HF (Yancy et al. 2013). According to the American Heart Association, the lifetime risk to develop HF is 20% with an average mortality of 50% after five years (Yancy et al. 2013). In Germany, this development is further driven by significant demographic changes such as an elevated life expectancy and a reduced mortality after myocardial infarction (Hasenfuß 2014).

Among the causes that can lead to HF, in heart muscle cells (cardiomyocytes), significant subcellular signalling and ultrastructural alterations have been reported that form a mechanistic basis for progressive pathophysiological remodeling and that disrupt normal organ function (Hasenfuß 1992). Cardiomyocytes are responsible for contractile force generation, which is essential for cardiac pump function, and ultimately controlled by the Excitation-Contraction Coupling (ECC) process (Bers 2002). In this context, both deficient intracellular Ca^{2+} handling and intracellular Ca^{2+} storage in the sarcoplasmic reticulum (SR) organelle are relevant since defects in either subcellular compartment can lead to arrhythmias and decrease contractile function (Gwathmey et al. 1987).

Since arrhythmias and HF frequently lead to death, there is an urgent need to better understand the underlying pathophysiological mechanisms.

1.2 Excitation and regulation of the ventricular cardiomyocyte

Cardiomyocytes, a major fraction of the cells in a human heart, are indispensable for contractile function (Jugdutt 2003). Excitation that eventually leads to contraction is initiated by the sinoatrial node (Irisawa et al. 1993). Moreover, specialised conductive cardiomyocytes (Purkinje fibres) coordinate electrical conduction, ensuring coordinated excitation of the heart tissue (Ideker et al. 2009). Electrical signals (action potentials) thereby

excite ventricular cardiomyocytes, which subsequently contract, altogether contributing to the hemodynamic work of the heart. During excitation, distinct ion currents are sequentially activated: sodium (Na^+), calcium (Ca^{2+}), and potassium (K^+) currents. Importantly, intracellular Ca^{2+} signals (Ca^{2+} transients), activated by Ca^{2+} Induced Ca^{2+} Release (CICR), ultimately underlie contractile activation of cardiomyocytes (Sandow 1952; Bers 2002).

Specifically, Excitation-Contraction Coupling (Figure 1) is accomplished by functional interactions between L-Type Calcium Channels (LTCC/Cav1.2) and Ryanodine Receptors type 2 (RyR2), Ca^{2+} release channels in subcellular nanodomains, localised in the sarcolemma (SL) and its transverse tubule invaginations (T-tubules or TTs) and the SR, respectively (Bers 2002). Voltage-dependent activation of Cav1.2 channels during depolarisation leads to an inward Ca^{2+} current in the dyadic subspace, the contact domain formed between TTs and junctional SR (jSR) terminals (Bers 2002). By this process, a relatively small amount of Ca^{2+} influx through Cav1.2 channels leads to opening of RyR2 channels, a process known as CICR (Fabiato and Fabiato 1978; Fabiato 1983). Finally, the Ca^{2+} release activates actomyosin cross-bridge cycling through Ca^{2+} binding to Troponin C (TnC), which initiates contraction (Ebashi et al. 1965; Collins et al. 1973).

Distinct mechanisms lead to the relaxation of cardiomyocytes: 1) Ca^{2+} re-uptake into the SR by the cardiac Sarco-/Endoplasmic Reticulum Ca^{2+} ATPase (SERCA2a) isoform, and 2) Na^+/Ca^{2+} exchange by the Na^+/Ca^{2+} exchanger (NCX) at the plasma membrane; additionally, the 3) Plasma Membrane Ca^{2+} ATPase (PMCA) and mitochondrial Ca^{2+} uptake contribute less than 1% to cytosolic Ca^{2+} extrusion in cardiomyocytes (Bers 2002; Prosser et al. 2010).

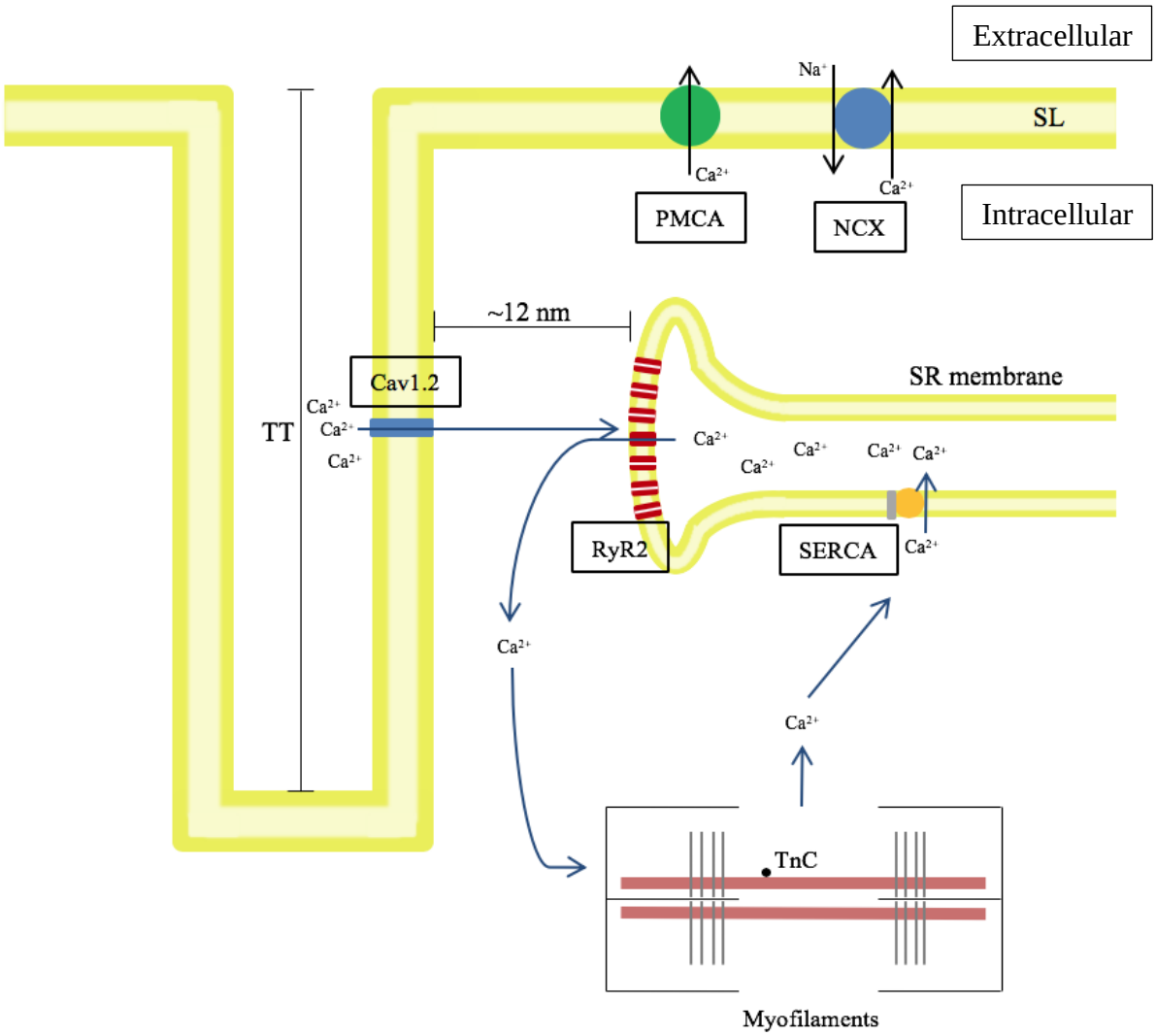

Figure 1: Cardiac ECC

Depolarisation leads to an inward Ca^{2+} current through the LTCC (Cav1.2) activation in the ~12 nm wide dyadic subspace formed between TTs and jSR terminals (Bers 2002; Hayashi et al. 2009). Next, Ca^{2+} binding opens RyR2 channels, which release a greater amount of Ca^{2+} stored in the SR (CICR) (Fabiato and Fabiato 1978). Finally, actomyosin crossbridge cycling cascade is activated by Ca^{2+} binding to TnC (Collins et al. 1973; Ebashi et al. 1965). For diastolic relaxation Ca^{2+} re-uptake into the SR by SERCA2a and Ca^{2+} extrusion via Na^{+}/Ca^{2+} exchange represent the major quantitative mechanisms. In addition, PMCA pumps Ca^{2+} to the extracellular space and mitochondrial Ca^{2+} uptake decreases cytosolic Ca^{2+} (not shown) (adapted from Bers 2002, Figure 1; Prosser et al. 2010, Figure 1).

1.3 The Cardiac Calcium Release Unit

As described above, cardiomyocytes require intracellular Ca^{2+} release from the SR for contractile activation (Fabiato and Fabiato 1978). Accordingly, the subcellular domains were termed Calcium Release Units (CRUs) and are essential for local CICR control (Stern 1992; Franzi-Armstrong et al. 1999). Earlier studies revealed important structural details of CRUs

(Bers and Stiffel 1993; Sun et al. 1995). For example, electron microscopy (EM) illustrated numerous electron-dense “foot” structures in the ~12 nm wide junctional subspace, subsequently identified as RyR2 channels (Inui et al. 1987; Sun et al. 1995). While similar structures have been identified in skeletal muscle, the ECC mechanism is fundamentally different (Fabiato 1983). In skeletal muscle, a different LTCC isoform (Cav1.1) is physically associated with RyR1 channels, such that Ca^{2+} release is activated by direct protein interactions in the absence of a Ca^{2+} inward current (Schneider and Chandler 1973). In addition, the stoichiometry of RyR channels relative to LTCCs in CRUs varies. Elegant freeze-fracture EM studies showed that cardiomyocytes use a ratio of approximately seven RyR2 channels per Cav1.2 in CRUs (Bers and Stiffel 1993; Sun et al. 1995).

More recent EM as well as superresolution microscopy studies describe further molecular details of CRUs as summarised in Kohl et al. (2013). Notably, RYR2 channels in the dyadic cleft vary significantly in size and morphology (Baddeley et al. 2009; Hayashi et al. 2009). The lateral distance between RyR2 clusters is typically above 100 nm and the number of RyR2 channels in a dyadic cleft varies considerably (Hayashi et al. 2009). About one third of dyadic clefts were found to contain less than 15 RyR2 channels (Hayashi et al. 2009). Finally, indirect immunofluorescence Stochastic Optical Reconstruction Microscopy (dSTORM) revealed irregular RyR2 cluster sizes (average ~107 nm), which were explained by varying numbers of RyR2 channels per cluster (Baddeley et al. 2009; Jayasinghe et al. 2018).

The dyadic structure and positioning of LTCC and RyR channels is likely to be important for efficient ECC (Wehrens et al. 2005). In contrast, defects in the CRU and TT structures may contribute to the development of HF (Song et al. 2006). Studies have, for example, shown a strong correlation between alterations in Ca^{2+} handling and pathophysiological processes such as abnormal contraction/relaxation mechanisms (Gwathmey et al. 1990; Hasenfuss et al. 1999).

Consequently, membrane proteins that may stabilise and shape CRU domains are of considerable interest. Among these, Junctophilin-2 (JPH2) and the muscle-specific Caveolin-3 (Cav3) isoforms and their changes are often investigated in the context of heart disease (Beavers et al. 2014).

1.4 Junctophilin – a CRU membrane tether

In 2000, Takeshima et al. identified several different JPH isoforms as members of a new family of membrane proteins (Takeshima et al. 2000). In the heart, JPH2 is now considered as an essential protein of CRUs, stabilising the ~12 nm wide junction between the SL and the SR membrane (Landstrom et al. 2014) (Figure 2). So far, four mammalian JPH isoforms are known to exist, which are expressed in different excitable cell types and to varying degrees (Beavers et al. 2014). JPH1 is mainly expressed in skeletal muscle cells, whereas JPH2 is expressed in both skeletal and heart muscle (Takeshima et al. 2000). JPH3 and JPH4 are mainly expressed in the brain (Nishi et al. 2003).

The structure of JPH isoforms is highly conserved (Garbino et al. 2009). Murine JPH isoforms range between 660 to 744 amino acids (Takeshima et al. 2000). In all JPH isoforms, conserved domains enable and maintain the alignment of contacts between the plasma membrane (PM) and the ER/SR (Takeshima et al. 2000) (Figure 2). At the N-terminus, 8 "Membrane Occupation and Recognition Nexus" (MORN) motifs mediate JPH binding to lipids in the intracellular leaflet of the PM (Takeshima et al. 2000; Bennett et al. 2013). These MORN motifs show the highest ratio of conserved amino acids between all JPH isoforms (76-90%), which indicates the capability of all JPH isoforms to bind the SL (Garbino et al. 2009). A central α-helical domain in the Jph2 protein is predicted to span some distance of the ~12 nm gap between the ER/SR and the PM and is thought to maintain the junctional width (Garbino et al. 2009). Further, the divergent region is much more variable between different JPH isoforms and is thought to form a flexible loop structure in the cytosol (Garbino et al. 2009). The variable domain was found to contain a calpain cleavage site at Arg-565/Thr-566 (Guo et al. 2015). Finally, the highly conserved C-terminal transmembrane (TM) domain of JPH2 anchors the molecule in the ER/SR membrane (Takeshima et al. 2000; Garbino et al. 2009).

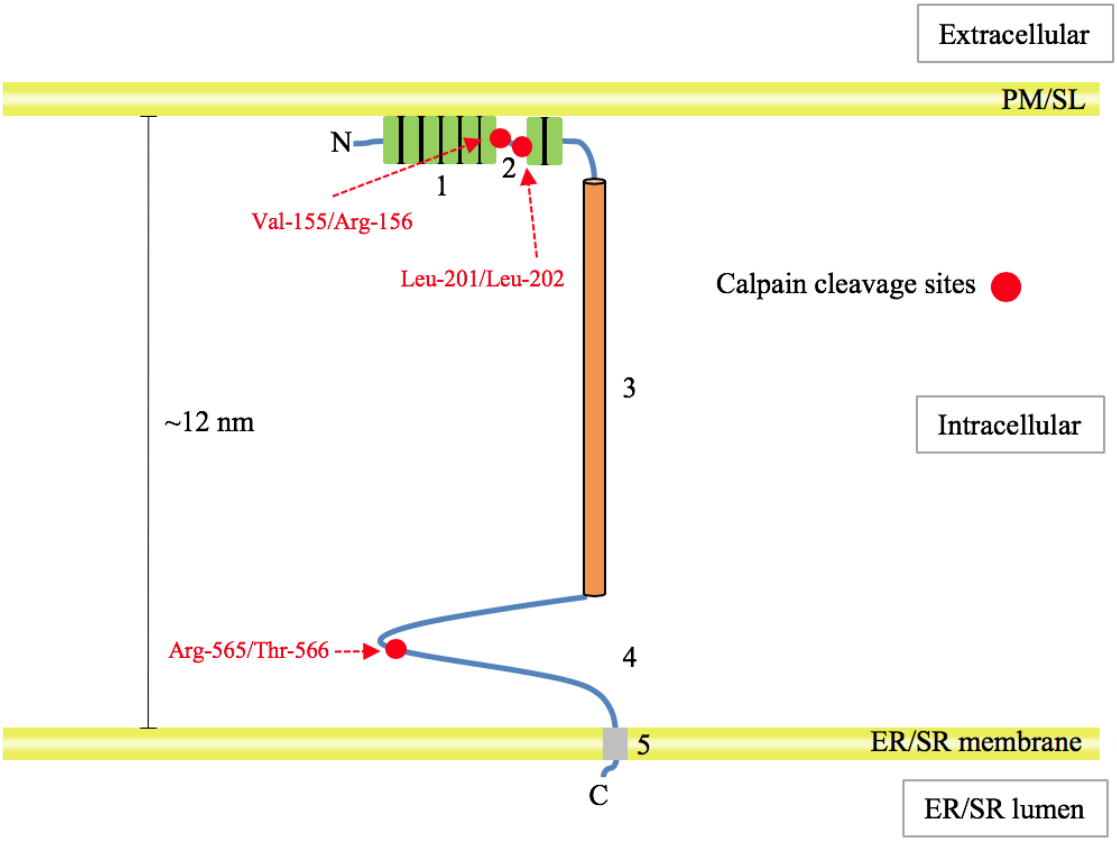

Figure 2: Scheme of JPH2 domain arrangement in the cardiac CRU.

The cartoon illustrates the JPH2 domain topology and protein domains. **1**: eight MORN motifs, **2**: joining region, **3**: α-helix, **4**: divergent region, **5**: C-terminal TM domain (adapted from Takeshima et al. 2000; Landstrom et al. 2014, Figure 3). The structural integrity of JPH2 and its specific conformation is thought to maintain CRU function (Landstrom et al. 2014). The N-terminal MORN motifs mediate the association with phospholipids in the SL (Takeshima et al. 2000). The α-helix spans some of the ~12 nm distance in the junctional cleft between the PM/SL and the ER/SR membranes (Garbino et al. 2009). The C-terminal TM domain functions as a tail-anchor of JPH2 in the ER/SR membrane (Takeshima et al. 2000). The calpain cleavage sites are shown in red (Guo et al. 2015).

1.4.1 Role of Junctophilin-2 dysregulation in heart failure

Several studies showed a functional correlation between HF and CRU disruption (Landstrom et al. 2011; Beavers et al 2013). A decreased level of JPH2 expression in murine cardiomyocytes, for example, was associated with ultrastructural CRU reorganisation and the loss of TTs (Minamisawa et al. 2004; Wagner et al. 2012). Furthermore, JPH2 mutations were found in patients with septal hypertrophic cardiomyopathy (HCM) and atrial fibrillation (Beavers et al. 2013; Quick et al. 2017).

Minamisawa et al. further showed that, to ensure the development of CRUs JPH2 was physiologically up-regulated during the post-natal development of healthy maturating

cardiomyocytes of murine hearts (Minamisawa et al. 2004). In contrast, the authors found a down-regulation of JPH2-mRNA of ~60% as well as a reduction in JPH2 expression of ~40% in a transgenic mouse model of HCM (Minamisawa et al. 2004). In addition, JPH2 expression was downregulated after myocardial infarction in mouse (Wagner et al. 2012) and in dilated human hearts (Zhang et al. 2013). By using transmission electron microscopy, the authors found a reduced number of dyadic TT/SR junctions (Zhang et al. 2013). Moreover, JPH2 down-regulation in dilated hearts was associated with an up-regulation of microRNA-24, which was shown to suppress JPH2 expression in cardiomyocytes (Xu et al. 2012; Zhang et al. 2013).

Landstrom et al. used JPH2 knockdown via transfection of shRNA targeted to the JPH2-mRNA in HL-1 cells, a cell line derived from murine atrial tissue (Landstrom et al. 2011). They observed an increase in HL-1 cell size, as well as an induction of pro-hypertrophic markers (i.e. increased expression of the Myosin Heavy Chain Beta isoform MYH7) along with malfunction of Ca^{2+} handling (Landstrom et al. 2011). Furthermore, human tissue from HCM hearts was investigated, where JPH2 was down-regulated (Landstrom et al. 2011). The authors therefore suggested that decreased JPH2 expression levels can be both, a cause or a consequence, of HF (Landstrom et al. 2011).

EM was also used to investigate the consequence of JPH2 knockdown through a shRNA targeting in adult mice at the level of structural CRU integrity (van Oort et al. 2011). While the total number of CRUs was significantly lower, an irregular and increased junctional width was found (van Oort et al. 2011). Moreover, JPH2 was found to bind to RyR2 channels (Beavers et al. 2013). Notably, JPH2 knockdown led to an increased diastolic Ca^{2+} leak through RyR2 channels, which was overall similar to observations reported in HF samples (Beavers et al. 2013).

In addition, a study by Wagner et al. quantified structural changes of the TT network in murine hearts, in conjunction with a significantly decreased Jph2 protein expression, 4 and 8 weeks after myocardial infarction (Wagner et al. 2012). Furthermore, altered localisation RyR2 clusters relative to Z-lines and dyssynchrony of local Ca^{2+} release were associated with a reduced expression of Jph2 (Wagner et al. 2012).

Besides the fact that reduced JPH2 levels can lead to TT remodeling and severe changes in Ca^{2+} handling, proteolysis of JPH2 was suggested as an additional mechanism for CRU dysfunction (Murphy et al. 2013). Intracellular Ca^{2+} overload, as observed in excessive

activated skeletal muscle cells and cardiomyocytes, is thought to activate increased cleavage of Jph-proteins through activation of Ca^{2+} dependent proteases (Murphy et al. 2013). In this context, Murphy et al. identified increased cleavage of JPH1 in human and rat skeletal muscles that were exposed to elevated Ca^{2+} concentrations (Murphy et al. 2013). They also found proteolytic fragments of JPH1 as well as a C-terminal domain that remains inserted in the SR after cleavage (Murphy et al. 2013). Finally, ischemia/reperfusion (I/R) studies in isolated rat hearts showed a reduction of full length JPH2 by ~25% (Murphy et al. 2013).

In summary, several studies found a correlation between HF remodeling and dysfunctional CRU domains. Further insights into the underlying ultrastructural and molecular mechanisms might be necessary, ultimately for at therapeutic translation relating to JPH2 changes and unknown protein interactions (Beavers et al. 2014; Landstrom et al. 2014).

1.4.2 Known interaction partners of Junctophilin

The role of Jph2 as a molecular tether between the PM/SL and the ER/SR membrane as the molecular basis for CRU stabilisation is now widely accepted (Beavers et al. 2014). Recent studies identified both, direct and indirect interaction partners of Jph-proteins (Beavers et al. 2014; Landstrom et al 2014). Even though Jph1 is mainly found in skeletal muscle cells, a significant amount is expressed in cardiomyocytes (Takeshima et al. 2000).

Immunoprecipitation experiments in cultured murine skeletal muscle cells (C2C12) revealed that JPH1, through binding of the joining region ($Jph2_{142-285}$), interacts with the α1-subunit of the LTCC (Cav1.1) channel (Golini et al. 2011). Additionally, Cav3 was described as a potential JPH1 interaction partner, an essential protein for the biogenesis of caveolae in muscle cells (Golini et al. 2011). Cav3 is also important for TT maturation (Galbiati et al. 2001). Hence, in skeletal muscle, it is assumed that these proteins form a macromolecular complex that includes RyR1 (Golini et al. 2011). The interaction between JPH1 and RyR1 might be conformation dependent and mediated by hyper-reactive thiols (functional SH groups) in JPH1 (Phimister et al. 2007). Thus, thiol modifications were suggested to play a role for the regulation of Ca^{2+} release during increased oxidative stress (Phimister et al. 2007). Interestingly, an association between Cav1.1, Cav3 and RyR1 was also shown for JPH2 in rabbit skeletal muscle cells (Golini et al. 2011).

In mouse ventricular myocytes, co-immunoprecipitation experiments showed a direct interaction between JPH2 and RyR2 (van Oort et al. 2011). Because JPH2 knockdown led to increased diastolic Ca^{2+} leak through RyR2, Jph2 may play an important role for the physiological closed state of RyR2 channels (van Oort et al. 2011). This functionally important RyR2 interaction was attributed to the Jph2 joining region in the cytosolic subspace (Beavers et al. 2013).

Jayasinghe et al. used superresolution dSTORM microscopy to gain insight into the nanoscale relationship between JPH2 and RyR2 (Jayasinghe et al. 2012). JPH2 and RyR2 were clustered in rat ventricular myocytes (Jayasinghe et al. 2012). The degree of signal colocalisation amounted to ~60-80% (Jayasinghe et al. 2012). Moreover, RyR2 clusters showed sharp edges with gaps, interspersed by JPH2 signals (Jayasinghe et al. 2012; Jayasinghe et al. 2018).

Li et al. showed that silencing of JPH1 expression in C2C12 myotubes leads to an impaired store-operated Ca^{2+} entry (SOCE), that plays a general role in Ca^{2+} homeostasis (Li et al. 2010). The authors suggested that this is caused by altered interactions of stromal interaction molecule 1 (STIM1) and Ca^{2+} release-activated Ca^{2+} modulator 1 (ORAI1), which physiologically mediate sarcolemmal Ca^{2+} influx to counter ER/SR Ca^{2+} depletion (Li et al. 2010). In addition, a direct isoform-specific interaction between JPH2 and the transient receptor potential cation channel type 3 (TRPC3), a cation channel important for the influx of extracellular Ca^{2+} and Na^{+}, was mediated by the JPH2 joining region as shown in rat skeletal muscle cells (Woo et al. 2009). Thereby, TRPC3 was suggested to also modulate RyR1 function (Woo et al. 2009). In contrast, an earlier study showed no such physical interaction between JPH1 and TRPC3 (Woo et al. 2008).

Finally, knockout of a phosphoinositide-3-kinase (PI3K) led to a reduced colocalisation of JPH2 and RyR2, as well as a relocation of JPH2 in mouse cardiomyocytes (Wu et al. 2011). Interestingly, an increase of perinuclear JPH2 clusters was detectable (Wu et al. 2011).
In summary, JPH1 was shown to interact with Cav1.1 (Golini et al. 2011), Cav3 (Golini et al. 2011), RyR1 (Phimister et al. 2007) and STIM1/ORAI1 (Li et al. 2010). JPH2 was shown to interact with: Cav1.1 (Golini et al. 2011), PS (Bennett et al. 2013), the RyR2 channel (van Oort et al. 2011), and TRPC3 (Woo et al. 2009).

1.4.3 Junctophilin in T-tubule development and pathological remodeling

JPHs contribute to muscle development through TT maturation and nature CRU coupling (Reynolds et al. 2013; Landstrom et al. 2014). JPH1 knockout mice showed a highly increased perinatal mortality, at least in part caused by disrupted CRUs in skeletal myofibres (Ito et al. 2001). Germ-line JPH2 knockout in mice was embryonically lethal and caused a significant increase of the junctional subspace, correlating with severe Ca^{2+} dysfunction (Takeshima et al. 2000).

By using JPH2 knockdown through shRNA in mice, Reynolds et al. showed that JPH2 is indispensable for TT sprouting during development (Reynolds et al. 2013). In this context, JPH2 knockdown by ~70% led to a significantly decreased TT density as well as a highly disorganised TT network at postnatal day 5 (Reynolds et al. 2013). The expression level of Cav3 and Myc box-dependent-interacting protein 1 (Bin1), proteins important for TT integrity that were shown to interact with JPH2, were not significantly altered (Reynolds et al. 2013). Thus, JPH2 may anchor nascent TT structures during cardiac maturation (Reynolds et al. 2013). In addition, JPH2 overexpression in the mouse heart resulted in accelerated TT maturation at postnatal day 8 (Reynolds et al. 2013).

Together, these studies indicated an important co-localisation function of JPH2 and RyR2 in CRUs in the context of TT development and remodeling (Landstrom et al. 2014). Yet, the mechanisms of Jph2 clustering in the context of junctional CRU domains remain unclear. Even though Jph2 is clearly indispensable for jSR contacts with the SL, it remains unclear how Jph2 clusters form, and ultimately may define the seed site for subsequent RyR2 clustering in cardiac and skeletal muscle CRUs (Jayasinghe et al. 2012).

1.5 STimulated Emission Depletion (STED) microscopy

Confocal laser scanning microscopy (LSM) is a well-established technique to study the signal patterns of fluorescently labelled proteins inside cells, although the spatial details are significantly limited by light diffraction (Kohl et al. 2013). As emitted light propagates as a wave and is subject to light diffraction, any fluorescent signal point source is subsequently modified by the optical point-spread-function (PSF) of a given LSM system in three dimensions (xyz) (Kohl et al. 2013). First described by Ernst Abbe, the minimal resolvable distance between two objects (d_{min}) depends on the wavelength of the emitted light (λ), the

refractive index (n) and the aperture angle of the objective lens sin(α) (Abbe 1873). According to Abbe's theory of light diffraction ($d_{min} = \lambda \times 2n \times \sin(\alpha)$) the maximal resolution that can be achieved amounts to 200-250 nm in x and y for modern LSM systems (Abbe 1873; Kohl et al. 2013). Consequently, two adjacent point emitters approximate the full width at half maximum (FWHM) of the PSF given by: $FWHM = 0.6 \times \lambda NA$ (Born and Wolf 2002). Consequently, two point emitters closer to each other cannot be resolved as separate signal objects in space (Born and Wolf 2002; see also Figure 3a). Fundamental developments, however, resulted in new superresolution technologies that overcome the diffraction barrier (Kohl et al. 2013).

So called super-resolution LSM techniques are based on the concept that fluorophores can be switched between a fluorescent (ON) and a non-fluorescent (OFF) ground-state. For this, STED microscopy uses a second laser beam with a doughnut shaped intensity and a minimal intensity zero at its centre, precisely layed over the excitation laser light path (Hell and Wichmann 1994; see also Figure 3b). The intensity crest of the doughnut shaped STED laser beam switches all peripheral fluorophores effectively to the dark state (OFF), significantly improving the effective spot size to 40 nm and less in cells under optimal conditions (Hell and Wichmann 1994; Kohl et al. 2013). STED microscopy therefore provides nanometric resolution and the advantages of a fast LSM approach, which is particularly advantageous for live cell imaging of metabolically sensitive cells (Kohl et al. 2013).

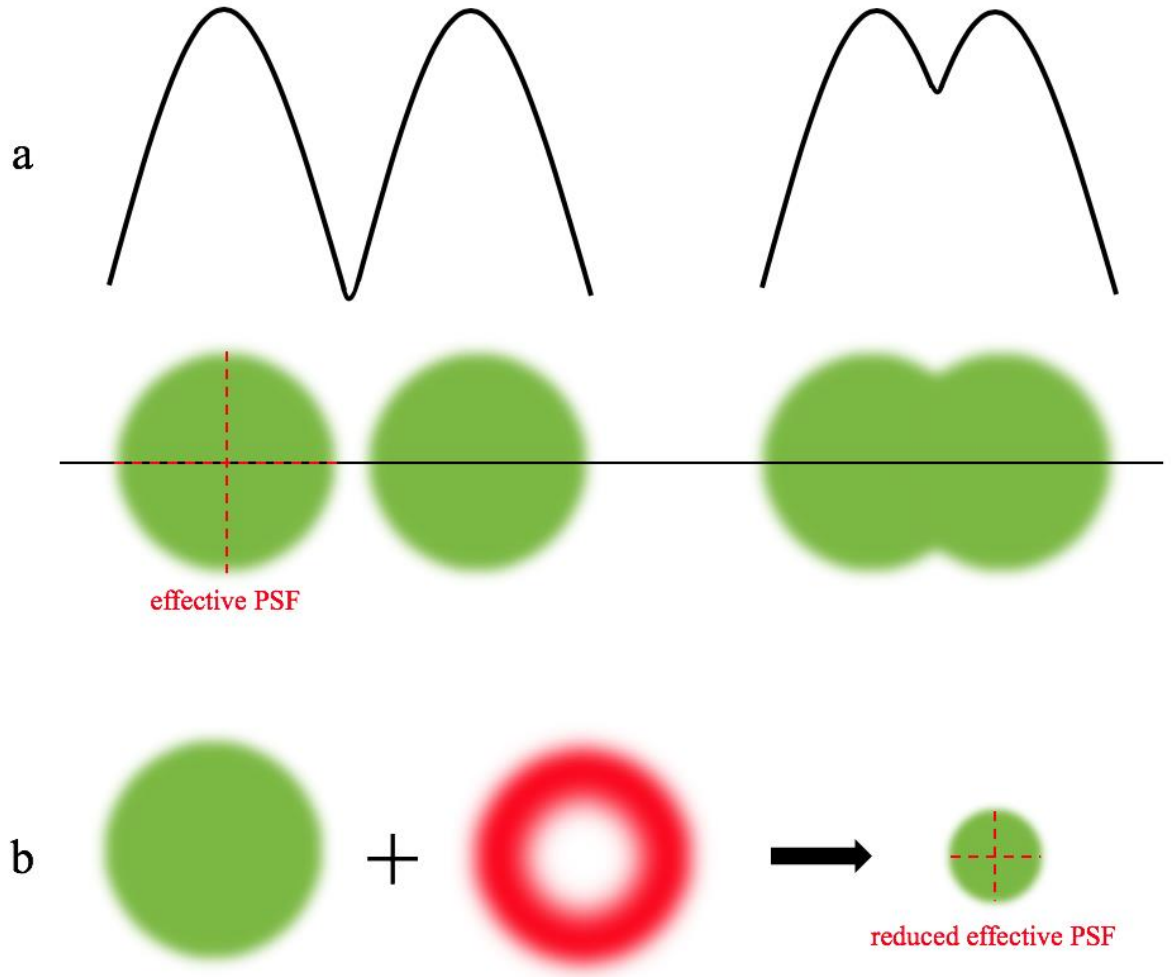

Figure 3: STED overcomes the diffraction barrier, reducing the effective PSF.

(a): The effective PSF provides an estimate for the expected distance that can be resolved between two light emitting fluorescent signals (green) to be distinguishable as single objects. **(b)**: STED uses a second doughnut shaped laser beam with a zero central intensity (far-red) that leads to a reduced size of the effective PSF thereby significantly increasing resolution (adapted from Kohl et al. 2013).

1.6 Objectives and Aims

This work was part of a collaborative research unit about modulatory units in HF (SFB 1002), with a focus on molecular CRU mechanisms and Jph2 clustering (project A06/A09). While Jph2 is necessary for the functional integrity of CRUs, the mechanisms of local Jph2 clustering are unclear (Jayasinghe et al. 2012). A multi-disciplinary approach was implemented that used i) novel Jph2 fusion proteins and engineered mutations in heterologous cell systems, ii) protein biochemistry and iii) super-resolution STED microscopy.

This project aims to analyse the subcellular distribution of Jph2 in clusters. Previous work has suggested relatively complex Jph2 and RyR2 cluster configurations. However, the driving forces that create local Jph2 clustering in ER/SR domain have not been studied (Jayasinghe et al. 2012). In conjunction with Jph2 clustering, TT remodeling and additional changes in HF need to be anticipated (Beavers et al. 2014; Landstrom et al. 2014).

Consequently, this study focuses on the subcellular distribution of novel JPH2 expression constructs in order to gain insight into the molecular clustering mechanisms, organelle specific targeting and the potential for Jph2 self-organisation in ER/SR membrane domains.

The following aspects are investigated in this research work:

Even though Jph2 changes in failing hearts have correlated with significant Ca^{2+} handling dysfunction (van Oort et al. 2011; Wagner et al. 2012), little is known about the local domain nature of these disease changes. The mechanisms of Jph2 self-organisation in clusters is currently unknown. Elucidation of the Jph2 clustering mechanism may potentially lead to new therapeutic strategies, i.e., curing CRU dysfunction in heart disease.

I set out to apply STED super-resolution microscopy to compare the local subcellular Jph2 cluster organisation between distinct cell types and also during skeletal muscle cell maturation. This analysis included both endogenous and heterologously expressed Jph2 and genetic variants. HEK293a cells were used to analyse heterologous Jph2 expression. Immature C2C12 skeletal myoblasts were subsequently differentiated into multinuclear C2C12 myotubes. Finally, neonatal rat cardiomyocytes (NRCM) were used as a cardiac cell culture model.

I have partly presented the contents of this dissertation during regular SFB1002 and IRTG1816 project meetings (Lehnart 2016; Zandt et al. 2017).

2. Materials and Methods

2.1 Materials

2.1.1 Chemicals

Table 1: Chemicals

Product	**Article/Company**	**Product number**
Bovine Calf Serum (BCS)	Fisher Scientific	SH30073.02
Dulbecco's Modified Eagle's Medium (DMEM)	Sigma-Aldrich	D6546
Fetal Bovine Serum (10%)	Sigma-Aldrich	F6178
L-alanyl-L-glutamine (1%)	Glutamax/Life Technologies	REF 35050-038
Horse Serum	Sigma-Aldrich	H1138
Poly-L-Lysine (0.01%)	Sigma-Aldrich	P4707
Lipofectamine 3000	Fisher Scientific	L3000-008
Antifade mountant without DAPI	ProLong gold/Invitrogen	P36934
Paraformaldehyde (PFA)	Sigma-Aldrich	158127
Penicillin-Streptomycin	Sigma-Aldrich	P4333
Phosphate Buffered Saline (PBS)	Invitrogen	10010-015
Triton X-100	Sigma-Aldrich	T9284
Trypan Blue Solution 0.4%	Sigma-Aldrich	T8154
Trypsin	Sigma-Aldrich	T3924

2.1.2 Cell culture materials

Table 2: Cell culture materials

Product	**Company**	**Product/Order number**
10 µl bevelled filter tips (sterile)	Star Lab	S1121-3810
100 µl bevelled filter tips (sterile)	Star Lab	S1120-1840
1000 µl bevelled filter tips (sterile)	Star Lab	S1122-1830
10 ml serologic pipettes	Sarstedt	86.1254.025
12 well cell culture plate	Greiner CELLSTAR	665180
5 ml serologic pipette	Sarstedt	86.1253.025
Cell culture flask (25 cm^2)	Sarstedt	83.3910
Cell culture flask (75 cm^2)	Sarstedt	83.3911
Cover clips 18 mm	Menzel (Thermo Scientific)	12382108
Eppendorf tubes (0.2 ml, 0.5 ml, 1.5 ml, 2.0 ml, 5.0 ml)	Eppendorf	
Microscope Slides	Superfrost Plus/Menzel (Thermo Scientific)	631-0099
Topcoat	Essence	-
Tube 15 ml	Sarstedt	62.554.002
Tube 50 ml	Sarstedt	62.547.254

2.1.3 Instruments

Table 3: Instruments

Application	Device	Company
STED and Confocal microscope system	Custom-developed Leica SP8 TCS STED microscope	Leica
Incubator	HERACELL 150i	Thermo Scientific
Laminar flow cabinet	Maxisafe 2020	Thermo Scientific
Vortex	Vortex	Star Lab
Centrifuge	HERAEUS MULTIFUGE X1R	Thermo Scientific
Waterbath	WNE14	Memmert
Light microscope	DM IRB	Leica
Pipettes (2.5 µl, 10 µl, 100 µl, 1000 µl)	Research Plus	Eppendorf

Table 4: Custom-developed Leica SP8 TCS setup for imaging

Elements	Company
100 × 1.4 NA objective (oil)	Leica
592 nm STED laser	Leica
775 nm STED laser	Leica
White light laser	Leica
Acousto-optical beam-splitter	Leica

2.1.4 Antibodies

2.1.4.1 Primary antibodies

Table 5: Primary antibodies

Primary antibody	Specification	Dilution	Company
Anti-Calreticulin	Rabbit, polyclonal	1:500	LifeSpan BioSciences
Anti-Caveolin 3	Rabbit, polyclonal	1:500	Abcam
Anti-c-myc	Mouse, monoclonal	1:500	Invitrogen
Anti-His-epitope	Mouse, monoclonal	1:500	ThermoFisher Scientific
Anti-Junctophilin-2	Rabbit, polyclonal	1:500	Invitrogen
Anti-Nogo	Goat, polyclonal	1:500	Santa Cruz
Anti-Ryanodine Receptor	Mouse, monoclonal	1:500	Thermo Scientific
Anti-Sec61b	Rabbit, polyclonal	1:500	Abcam
Anti-V5	Mouse, monoclonal	1:500	Invitrogen
Anti-V5	Rabbit, polyclonal	1:500	Sigma-Aldrich
Anti-ERGIC-53/p58	Rabbit, polyclonal	1:500	Sigma-Aldrich

2.1.4.2 Secondary antibodies

Table 6: Secondary antibodies

Secondary antibody	Specification	Dilution	Company
Anti-rabbit AlexaFluor 488	Donkey	1:1000	Life Technologies
Anti-mouse Abberior Star 488	Goat	1:1000	Abberior
Anti-goat AlexaFluor 488	Donkey	1:1000	Life Technologies

Secondary antibody	Specification	Dilution	Company
Anti-mouse AlexaFluor 568	Goat	1:1000	Life Technologies
Anti-goat AlexaFluor 568	Donkey	1:1000	Life Technologies
Anti-rabbit Abberior Star 635P	Goat	1:1000	Abberior

2.1.5 Membrane stain

Table 7: Membrane stain

Stain	Excitation/Emission	Company
Wheat Germ Agglutinin (WGA) AlexaFluor 633 Conjugate	632/647	Invitrogen

2.1.6 Plasmids

2.1.6.1 V5-APEX-JPH2 plasmids

The plasmids contain the pcDNA3 backbone and sub-cloned murine JPH2 cDNA. V5, which is an established epitope-tag recognised by a high-affinity antibody, as well as ascorbate peroxidase (APEX), which can be utilised for proximity proteomics, were used as N-terminal tags. APEX was derived from pcDNA3-mito-APEX (Addgene #42607, Rhee et al. 2013). All plasmids were kindly provided by Dr. G. Weninger (AG Lehnart, Heart Research Center Göttingen).

Table 8: pcDNA3-V5-APEX-JPH2 plasmids

Name of plasmid (vector backbone: pcDNA3)	**Construct**	**JPH2 truncation**
pcDNA3-V5-APEX-JPH2 full-length (FL)	V5-APEX tagged FL-JPH2 (V5-FL-JPH2)	Full length JPH2 without any truncation (1-696)
pcDNA3-V5-APEX-JPH2 (N-terminally truncated; includes divergent region + transmembrane domain; devoid of MORN-motifs, α-helix and joining region)	V5-APEX tagged truncated JPH2 (V5-ΔDR-TM-JPH2)	Transmembrane (TM) domain plus divergent region (433-696)
pcDNA3-V5-APEX-JPH2 TM only	V5-APEX tagged TM only JPH2 (V5-ΔTM-JPH2)	Only TM domain (670-696)

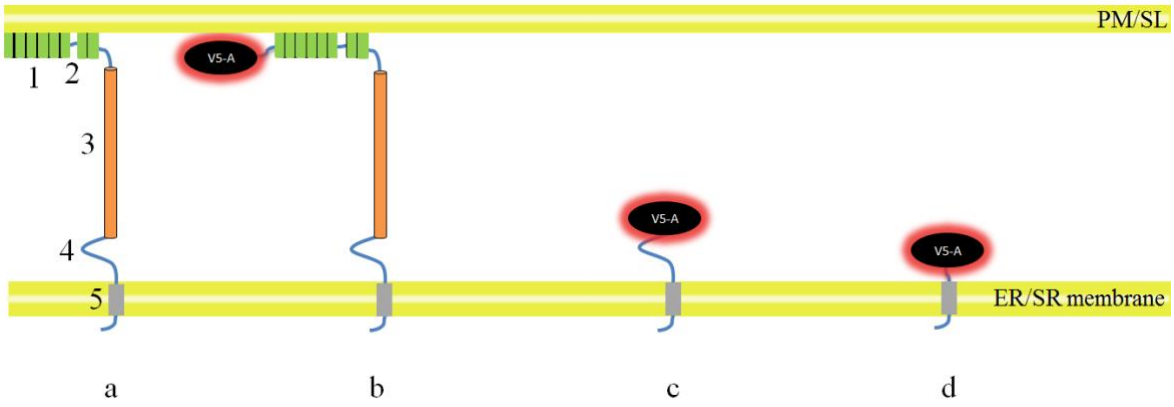

Figure 4: Topology of different JPH2 constructs.

(a): Illustration of JPH2 without the fusion tag (**1**: MORN motifs, **2**: joining region, **3**: α-helix, **4**: divergent region (DR), **5**: transmembrane (TM) domain). **(b)**: V5-full length (FL)-JPH2 (Δ0), **(c)**: V5-ΔDR-TM-JPH2 (Δ1-432), **(d)**: V5-ΔTM-JPH2 (Δ1-669). A = engineered Ascorbate Peroxidase (APEX): red indicates reactive cloud used for proximity proteomics (not investigated here).

In the following, the construct names will be termed without using “APEX”.

2.1.6.2 pcDNA3-rsEGFP2-His6-JPH2 plasmids

The different pcDNA3-rsEGFP2-His6-JPH2 plasmids included designed mutations in the TM domain. In detail, recombinant JPH2 was N-terminally fused to a His6-tag followed by rsEGFP2, a photoswitchable fluorescent protein (Grotjohann et al. 2012). The intention of the C678A mutation was based on a study by Kaether et al. who showed that the ER protein "PS enhancer 2" remained in the ER via retention (Kaether et al. 2007). Moreover, C-terminal mutation of asparagine to lysine led to a disturbed retention mechanism (Kaether et al. 2007).

Through a C-terminal extension of the pcDNA3-His6-rsEGFP2-FL-JPH2 plasmid through additional leucines (4L and 8L) a possible relocation to the PM/SL was investigated. All plasmids (Table 9) were kindly provided by Dr. G. Weninger (AG Lehnart, Heart Research Center Göttingen).

Table 9: pcDNA3-His6-rsEGFP2-JPH2 plasmids

Plasmid name (vector backbone: pcDNA3)	**Description**
pcDNA3-His6-rsEGFP2-TM-JPH2-C678A	Cysteine to arginine mutation at position 678, TM only
pcDNA3-His6-rsEGFP2-TM-JPH2-C678A-N684L	Cysteine to arginine mutation at position 678 and asparagine to lysine mutation at position 684, TM only
pcDNA3-His6-rsEGFP2-TM-JPH2-N684L	Asparagine to leucine mutation at position 684, TM only
pcDNA3-His6-rsEGFP2-FL-JPH2-4L	C-terminal extension through additional 4 leucines at position 683, FL construct
pcDNA3-His6-rsEGFP2-FL-JPH2-8L	C-terminal extension through additional 8 leucines at position 683, FL construct

2.1.7 Cell systems

Table 10: Cell systems

Cell system	Company/Product	Description
Human Embryonic Kidney cells (HEK293a)	ATCC/CRL-1573	Human cell line transfected with adenovirus 5
C2C12	ATCC/CRL-1772	Murine myoblasts derived from thigh muscle. This cell line is able to differentiate
Neonatal rat cardiomyocytes (NRCM)	(Isolated by Sebastian Pasch, AG Lutz, Department of Pharmacology, University Medical Centre Göttingen)	Primary neonatal rat cardiomyocytes

2.1.8 Growth media

2.1.8.1 Complete growth medium for HEK293a and C2C12 myoblasts

450 ml Dulbecco's Modified Eagle's Medium (Sigma-Aldrich; see also Table 1)

+ 50 ml Fetal Bovine Serum (Sigma-Aldrich)

+ 5 ml L-alanyl-L-glutamine (Glutamax, Life Technologies)

+ 5 ml Penicillin/Streptomycin (Sigma-Aldrich)

2.1.8.2 C2C12 differentiation medium

500 ml Dulbecco's Modified Eagle's Medium (Sigma-Aldrich; see also Table 1)

+ 10 ml Horse Serum (Sigma-Aldrich)

+ 5 ml Penicillin/Streptomycin (Sigma-Aldrich)

2.1.9 Blocking buffer and permeabilisation

9 ml Phosphate Buffered Saline (Invitrogen; see also Table 1)

+ 1 ml Bovine Calf Serum (Fisher Scientific)

+ 20 µl Triton X-100 (Sigma-Aldrich).

2.2 Methods

2.2.1 Cell culture

All cell culture experiments used a laminar flow cabinet (Maxisafe 2020, Thermo Scientific) under sterile conditions (with autoclaved vessels and pipettes).

2.2.1.1 Cultivation of HEK293a cells

HEK293a cells were cultivated under standard condition (37°C, 90% humidity and 5% CO_2) in cell culture flasks (75 cm_2) with 10 ml growth medium (see 2.1.8.1). The cells were split at a density of ~70%. For this, the cells were washed with PBS and detached with 400 µl trypsin-EDTA for 1 minute at 37°C. To inactivate trypsin, 10 ml complete growth medium (see 2.1.8.1) was added. Next, the solution was diluted (1:10) by adding further complete

growth medium and subsequently added to new flasks (10 ml in 75 cm² flask). The growth medium (2.1.8.1) was renewed every 2 days.

For transfection experiments the solution was centrifuged (500 rounds per minute for 5 minutes). Next, 10 ml complete growth medium (see 2.1.8.1) was added. Finally, the solution was transferred into a 12-well plate with a cell density of 20,000 cells per well.

2.2.1.2 Cultivation of C2C12 myoblasts

C2C12 myoblasts were cultivated under standard condition in a cell culture flask (75 cm²) with 10 ml complete growth medium (see 2.1.8.1). At a density of ~50% the myoblasts were washed with PBS and subsequently detached by adding 400 µl trypsin-EDTA (1 minute at 37°C). Next, 200 µl of the solution was diluted (1:50) by adding 10 ml complete growth medium and transferred to new flasks (75 cm²). For transfection experiments the myoblasts were seeded into a 12-well plate with a density of 20,000 cells per well.

2.2.1.3 Differentiation of C2C12 myoblasts

C2C12 murine myoblasts were differentiated by serum depletion and ~70% cell confluence according to the protocol by Lawson and Purslow (Lawson and Purslow 2000).

In short, myoblasts were seeded into a 12-well plate at a mean density of 150,000 cells per well. After 24 hours incubation under standard condition (37°C, 90% humidity and 5% CO_2) the adherent growth and confluent density of the myoblasts were visualised with a light microscope (DM1000, Leica). Subsequently, the cells were incubated for up to 7 days. Differentiated myotubes at day 7 showed an increased size and a brick like morphology. Furthermore, multiple nuclei per single cell were confirmed as expected when several myoblasts fuse into a singular myotube.

2.2.1.4 Cell counting by Neubauer chamber

A Neubauer chamber was used to determine the number of cells. For this, 50 µl cell suspension was diluted in growth medium and mixed with 50 µl trypan blue (1:1). Next, the solution was transferred into a Neubauer chamber. Subsequently, cells in a grid of 8 large squares were counted. Considering the given dilution (1:2), the following formulas were used to determine the number of cells in the solution:

Sum of cells counted in 8 squares ÷ 8 = mean of cells per square volume (10 µl)

Mean of cells per square × 100 = cells per ml

Cells per ml × total volume = total cell amount in suspension

2.2.1.5 Transfection protocol

Cells were seeded into a 12-well plate with a mean density of 20,000 cells per well. For this, glass coverslips were coated with Poly-L-Lysine and loaded into the wells. Transfection was started after 24 hours of cell incubation under standard condition (37°C, 90% humidity and 5% CO_2). For transfection Lipofectamine 3000 (3µl per µg DNA) was used. 5 hours were determined as a suitable expression time (see 3.1).

In detail, 59 µl DMEM (without supplement) was mixed with 10 µl P3000 and 3 µg of plasmid DNA. Subsequently, the solution was incubated for 5 minutes at room temperature. Then, 200 µl DMEM was added to give "solution 1" (total volume = 263 µl). At the same time, 260 µl DMEM was mixed with 3 µl Lipofectamine and incubated for 5 minutes at room temperature ("solution 2"). As recommended by manufacturer (Fisher Scientific) both solutions were mixed and incubated for 45 minutes at room temperature. Finally, 500 µl of the resulting solution was added to the cells and incubated for 5 hours (37°C, 95% humidity and 5% CO_2).

2.2.1.6 Transfection of differentiated C2C12 myotubes

The transfection protocol for C2C12 myoblasts was adapted for differentiated myotubes. To transfect differentiated myotubes a protocol was established. For this, the transfection protocol (2.2.1.5) and the differentiation protocol (2.2.1.3) were integrated.

In detail, cells were seeded into 12-well plates with a density of 150,000 cells per well. After 3-4 days of incubation under standard condition (37°C, 95% humidity and 5% CO_2) early differentiation was confirmed by light microscopy (DM1000, Leica) considering the following criteria: 1) cell size and 2) brick like morphology. Based on the idea that a large percentage of neighbouring cells were not fully differentiated at this state, the transfection protocol was started (see "Stadium 2" in Figure 5). Finally, cells were incubated for at least three more days. Cells differentiation was confirmed thereafter (Figure 5).

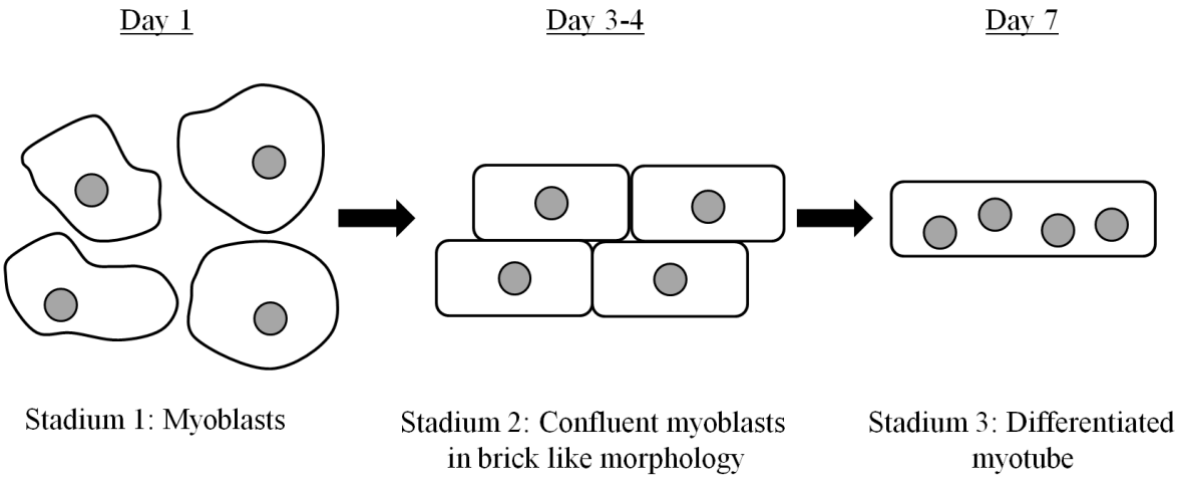

Figure 5: Scheme of C2C12 myoblast differentiation

Stadium 1: According to the protocol by Lawson and Purslow, C2C12 myoblast differentiation was initiated by serum depletion (Lawson and Purslow 2000; see also 2.1.8.2). **Stadium 2**: C2C12 myoblasts aligned at cell borders after 3-4 days while growing more confluent. This time point was chosen for transfection. **Stadium 3**: After 7 days, differentiated myotubes were visualised.

2.2.2 Indirect Immunofluorescence

Indirect immunofluorescence (IF) based on primary and secondary antibodies was used. Primary antibodies are specific for a particular protein epitope and in return get detected by secondary fluorescently labelled antibodies. Specific laser beam wavelengths were used to excite the fluorophores (Figure 6) and their emitted light (fluorescence) was then spectrally separated and detected by a fluorescent microscope (see also 2.1.4).

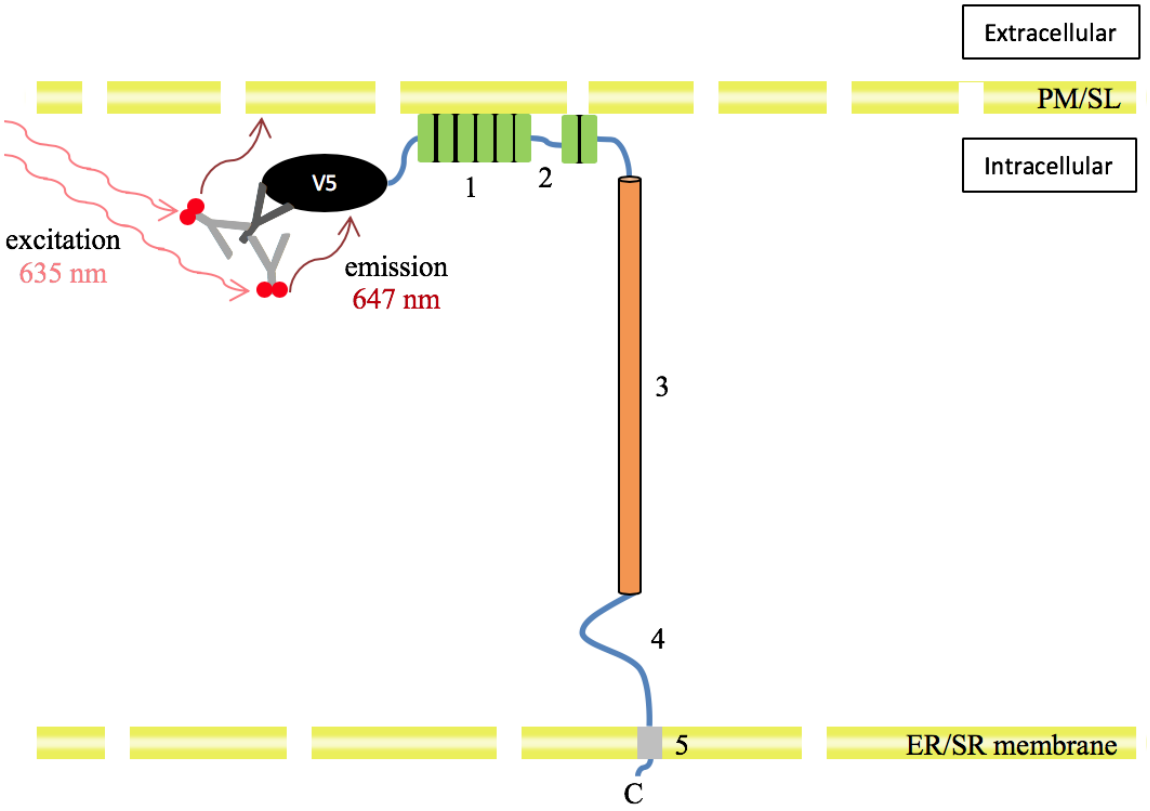

Figure 6: Indirect IF of V5-FL-JPH2

The cartoon shows the specific anti-V5 antibody (i.e. rabbit anti-V5 antibody, Sigma-Aldrich; see also Table 5) attached to the high affinity V5-tag (Rhee et al. 2013) of the V5-FL-JPH2 expression construct, which in return is detected by fluorescently labelled secondary antibodies (i.e. anti-rabbit Star 635P, Abberior; see also Table 6). The excitation of fluorophores (635 nm wavelength) leads to an emission at a defined wavelength (647 nm) and consequently allows for indirect localisation of the V5 tag (adapted from Fritschy and Härtig 2001; Landstrom et al. 2014, Figure 3). JPH2 topology: **1**: MORN motifs, **2**: joining region, **3**: α-helix, **4**: divergent region, **5**: TM domain. The PM/SL is discontinuous due to permeabilisation with Triton X-100 (see also 2.1.9).

2.2.2.1 Immunofluorescence staining protocol

The cells (HEK293a, C2C12, NRCM) were carefully washed with 37°C warm PBS and subsequently fixed with 4% PFA for 10 minutes. Next, the cells were washed with blocking buffer that included Triton X-100 (see 2.1.9) and blocked for 30 minutes at room temperature. Subsequently, the primary antibodies were added for 24 hours at 4°C. Then, cells were washed three times with blocking buffer (2 x 1 minute and 1 x 10 minutes). Finally, secondary antibodies were added for three hours at room temperature (in a dark environment to protect the fluorophores) and washed three times with blocking buffer (2 x 1 minute and 1 x 10 minutes) and two times with PBS. Thereafter, cells were mounted with

antifade mountant (Prolong gold without DAPI, Invitrogen; see also Table 1). The coverslips were sealed with nail polish after 48 hours.

2.2.3 Confocal Laser Scanning Microscopy (CLSM)

Fluorescence microscopy with light of a specific wavelength was used for dye excitation. In detail, the laser beam was focused and the confocal volume was scanned through the sample to detect the distribution of fluorophores. The pinhole placed before the detector was used to avoid out-of-focus fluorescence. A lateral resolution of ~250 nm (in x and y) was achieved and confirmed by imaging 100 nm tetraspeck beads (#T7279, Invitrogen).

For CLSM, a customised STED microscope (SP 8 TCS, Leica) was used. The confocal function was especially important to select the region of interest (ROI) prior to STED imaging and to reduce bleaching artefacts. Based on the Nyquist criterion of at least 2.3 pixels within the resolution, the pixel size was set at 80 nm for confocal imaging. To minimise crosstalk between two spectrally distinct dyes, sequential line scanning was chosen for image acquisition (sequential line scanning means that excitation and detection of different dyes occur independently on a line-by-line basis). Proprietary software was used (LAS X, Leica) and images were saved as ".lif"-files. For analysis with Fiji/ImageJ (see 2.2.5), files were exported as ".tif"-files.

2.2.4 STED microscopy

A customised STED microscope (SP8 TCS, Leica) was used to increase lateral resolution (~60 nm in muscle cells). For specific setup components, please refer to Table 4.

The setup parameters were adjusted according to the dye properties, including spectral characteristics, quantum yield and photostability. Setup parameters were empirically tested and routinely reproduced for comparative analysis.

2.2.5 Image analysis

FIJI, a Java-based free image processing and analysis software (https://fiji.sc) was used as platform for image analysis. For detailed information of plugins, please refer to: http://imagej.net/Category:Plugins.

2.2.5.1 Image normalisation

The image brightness was intensity-normalised to the 99.99 percentile rank (command: enhance contrast to 0.01% saturation). To minimise artefacts from small local signal fluctuations, signals were smoothed with a median filter (r = 1). Background signals were subtracted to improve image segmentation using the "rolling ball" algorithm.

2.2.5.2 Image segmentation, area fraction and particle size analysis

Object and background signals were defined by an image histogram-based approach ("Otsu Auto threshold"; see Figure 7b). Subsequently, the area fraction was determined as signal area divided by ROI area (see 2.2.5.6). Segmented objects were further used to calculate the frequency of particle sizes.

2.2.5.3 Peak intensity analysis

Bright local signal peaks were defined as pixels of at least 10 grey scale units brighter signal intensity (8-bit, normalised images) compared to neighbouring pixels using the "Find Maxima" (Fiji) function. These local maxima were further analysed by applying the "Nearest Neighbour Distance" plugin (see 2.2.5.4).

2.2.5.4 Nearest neighbour distance (NND) analysis

The distance between local signal peaks was calculated using the "Nearest Neighbour Distance" plugin.

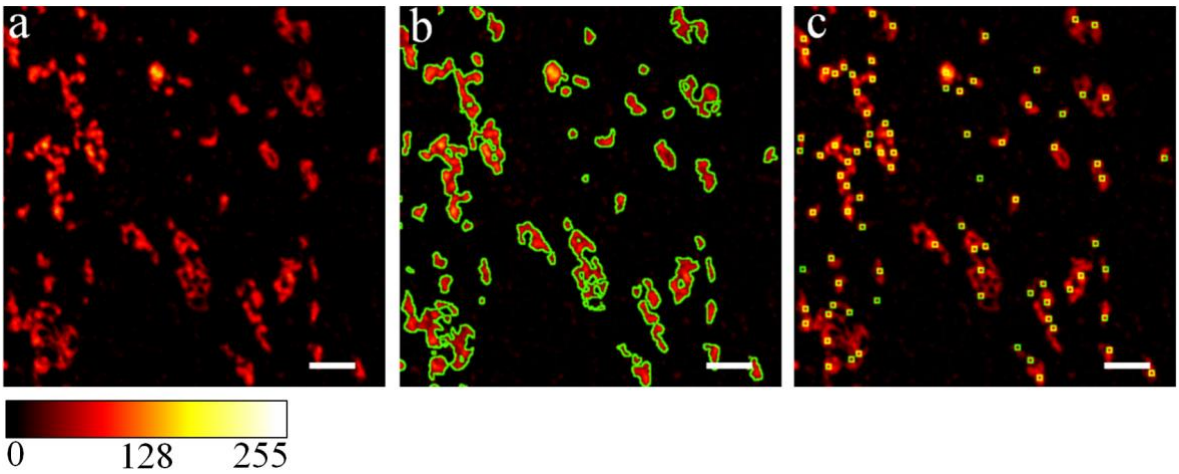

Figure 7: STED imaging and analysis of V5-FL-JPH2 expressed in a C2C12 myoblast

(a): The STED image shows the V5-FL-JPH2 signals in a C2C12 myoblast (detected by mouse anti-V5 and anti-mouse AlexaFluor 568). **(b)**: Image objects (green circumference lines) were identified by Otsu Auto thresholding. **(c)**: Bright local signal peaks were identified by the "Find Maxima" function in Fiji. The lookup table indicates the brightness rank of signals. Scale bars: 1 µm. For detailed information about antibody dilution, please refer to Materials and Methods (2.1.4).

2.2.5.5 Skeleton analysis

Network-like signal structures in images were extracted and their signal patterns were analysed. Based on the segmented image objects, the "Skeletonize" plugin was used to extract binary skeletons. Skeleton length was calculated by the "Analyze Skeletons" plugin in Fiji.

2.2.5.6 Region of interest

Analysis was performed for relevant regions of the ER/SR defined by the ROI. In general, nuclear signals and regions devoid of cells were excluded from analysis.

2.2.5.7 Statistics

When comparing two groups, statistical significance was tested by using either the unpaired two tailed t-test for normally distributed statistical populations or the Mann-Whitney test for non-normally distributed data sets. For comparison of multiple groups, a Kruskal-Wallis ANOVA test was applied, followed by a post-hoc test as appropriate (Tukey's test for parametric data; Mann-Whitney test with Bonferroni correction for non-parametric data). Statistical testing was performed with Microsoft Office Excel 2010 and OriginLab (Origin 9). A p-value < 0.05 was accepted as significant. All data are presented as mean ± standard deviation.

2.2.6 Drift correction

Chromatic aberration was tested based on imaging 100 nm tetraspeck beads (#T7279, Invitrogen) using the same parameters as for sample imaging. Consequently, a two-colour image drift was corrected with difference measured to optimise signal overlap between the different colour channels and as described previously (Hebisch et al. 2017).

3. Results

The intracellular distribution of different JPH2 fusion constructs (see 2.1.6.1) was analysed in different cell systems (HEK293a, C2C12, NRCM; see also 2.1.7) to gain insight into the mechanism of JPH2 clustering at specific subcellular locations and its distribution throughout the ER/SR. C2C12 myoblasts were used to compare the JPH2 expression and distribution pattern during differentiation of the clonal skeletal muscle-derived cells.

The hypothesis was that the C-terminal domain of JPH2 (TM domain) is not sufficient to mediate subcellular cluster formation. Accordingly, N-terminal truncation constructs of murine JPH2 were expressed to probe for changes in intracellular JPH2 distribution and/or cluster formation. The hypothesis was further tested by comparing V5-tagged full-length JPH2 (V5-FL-JPH2) against two deletion constructs (V5-ΔDR-TM-JPH2 and V5-ΔTM-JPH2; see also 2.1.6.1). For subcellular visualisation of JPH2 clusters, superresolution STED microscopy was employed as shown in Figure 8.

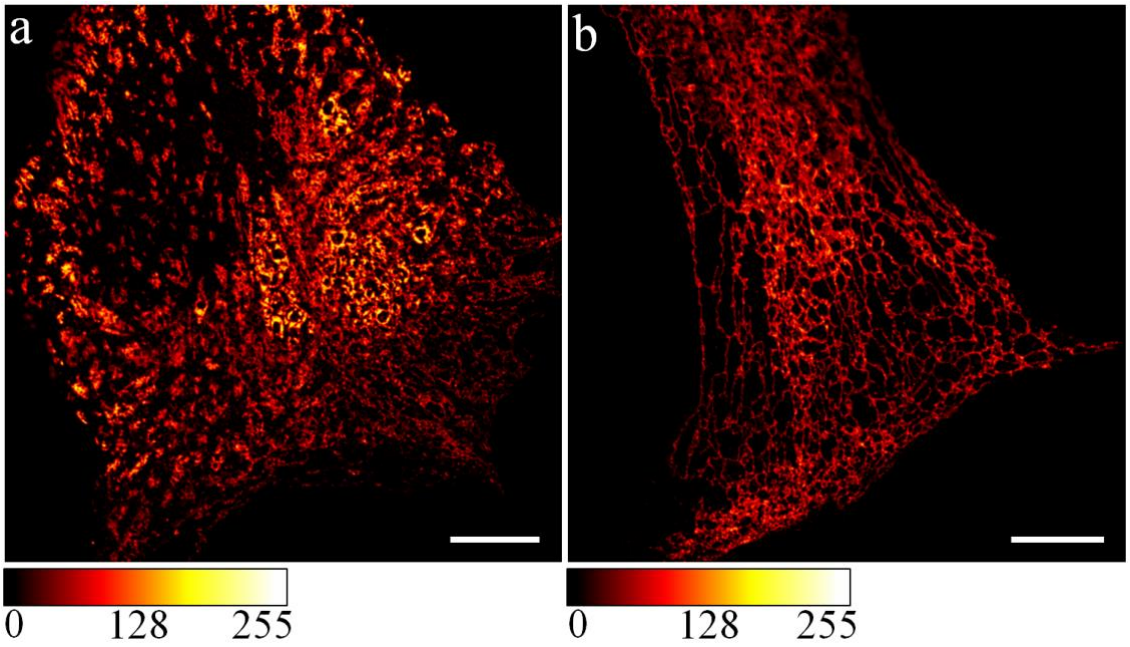

Figure 8: STED image of V5-FL-JPH2 and V5-ΔTM-JPH2 expressed in C2C12 myoblasts

STED images show representative overviews of the subcellular distribution of **(a)**: V5-FL-JPH2 and **(b)**: V5-ΔTM-JPH2 expression in C2C12 myoblasts (day 2) detected by mouse anti-V5 and anti-mouse AlexaFluor 568. Note that the signal pattern of the visualised clusters and the localisation in the ER/SR differs. The V5-ΔTM-JPH2 signal appears more ubiquitous, whereas V5-FL-JPH2 is typically restricted to isolated clusters. The lookup table indicates the brightness by colour. Scale bars: 5 µm. For detailed information about antibody dilution, please refer to Materials and Methods (2.1.4).

3.1 Sufficient signal strength for IF detection after five hours of V5-JPH2 construct expression

On the one hand, IF detection requires a minimum level of protein expression to visualise specific signals. On the other hand, prolonged overexpression can result in exogenous protein excess and unspecific aggregation. Accordingly, a sufficiently long, yet not too long expression time for JPH2 constructs was determined. The following time points were chosen for comparison: 5 hours – 10 hours – 24 hours – 48 hours. Thereafter, the cells (HEK293a and C2C12 myoblasts) were fixed and labelled by the established JPH2 IF protocol (see 2.2.2.1).

Five hours of V5-FL-JPH2 and V5-ΔTM-JPH2 (Figure 9) expression resulted in sufficient signal strength and detail for STED imaging as evidenced by distinct subcellular domains and signal levels.

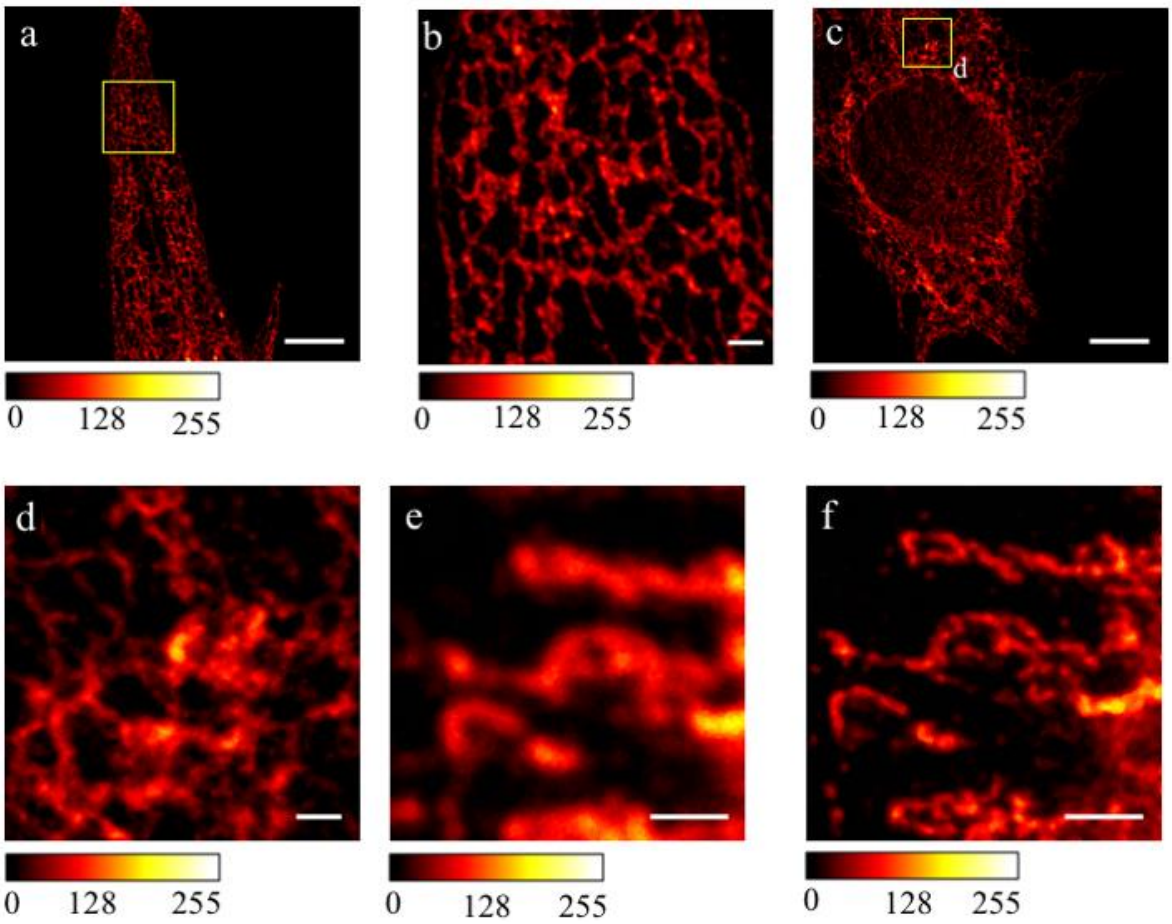

Figure 9: STED imaging after 5 and 10 hours V5-JPH2 construct expression in C2C12 myoblasts

The images visualise IF detection of V5-ΔTM-JPH2 (Δ1-669) in C2C12 myoblasts (day2) after 5 hours as well as 10 hours expression time (detected by mouse anti-V5 and anti-mouse AlexaFluor 568; see also 2.1.4). **(a)**: The signal pattern after 5 hours expression time shows a reticular pattern with distinct domains at a high contrast. Different signal levels and small structures can be distinguished. Scale bar: 5 µm. **(b):** Inset from (a). Scale bar: 1 µm. **(c)**: 10 hours expression time resulted in spatially larger and blurred signals. Scale bar: 5 µm. **(d)**: Inset from (c). Scale bar: 1 µm. **(e):** Detail of confocal image of clustered structures in a C2C12 myoblast expressing V5-FL-JPH2. Scale bar: 1 µm. **(f):** STED image of the same detail as (e), shows the advantage of STED superresolution microscopy in comparison with confocal imaging, which is limited by light diffraction. Scale bar: 1 µm. The lookup table indicates the brightness by colour. For detailed information about antibody dilution, please refer to Materials and Methods (2.1.4).

3.2 Visualisation and correlation of the ER morphology

Previously established markers of the ER/SR were tested in HEK293a, C2C12 myoblasts and NRCM with the aim to visualise ER/SR organelle structure and to confirm the specific localisation of V5-JPH2 constructs.

For this, KDEL-Crimson transfection was used, which is a protein that is retained in the ER/SR and linked to a fluorophore for detection. ER sheets and tubules were visualised in HEK293a, C2C12 and NRCM cells (Figure 10). As expected, ER sheets were visualised perinuclear and in peripheral ER/SR areas near the PM/SL. Moreover, ER tubules were found throughout the reticular network. Even though the exact proportion of sheets versus tubules varied between HEK293a, C2C12 and NRCM cells, both prototypical ER/SR domains were clearly visible. In contrast, IF imaging of the molecular markers Reticulon-4 (Nogo), Sec61 translocon beta (Sec61b) and Calreticulin did not show the clear preference for sheet-like or tubular signal patterns.

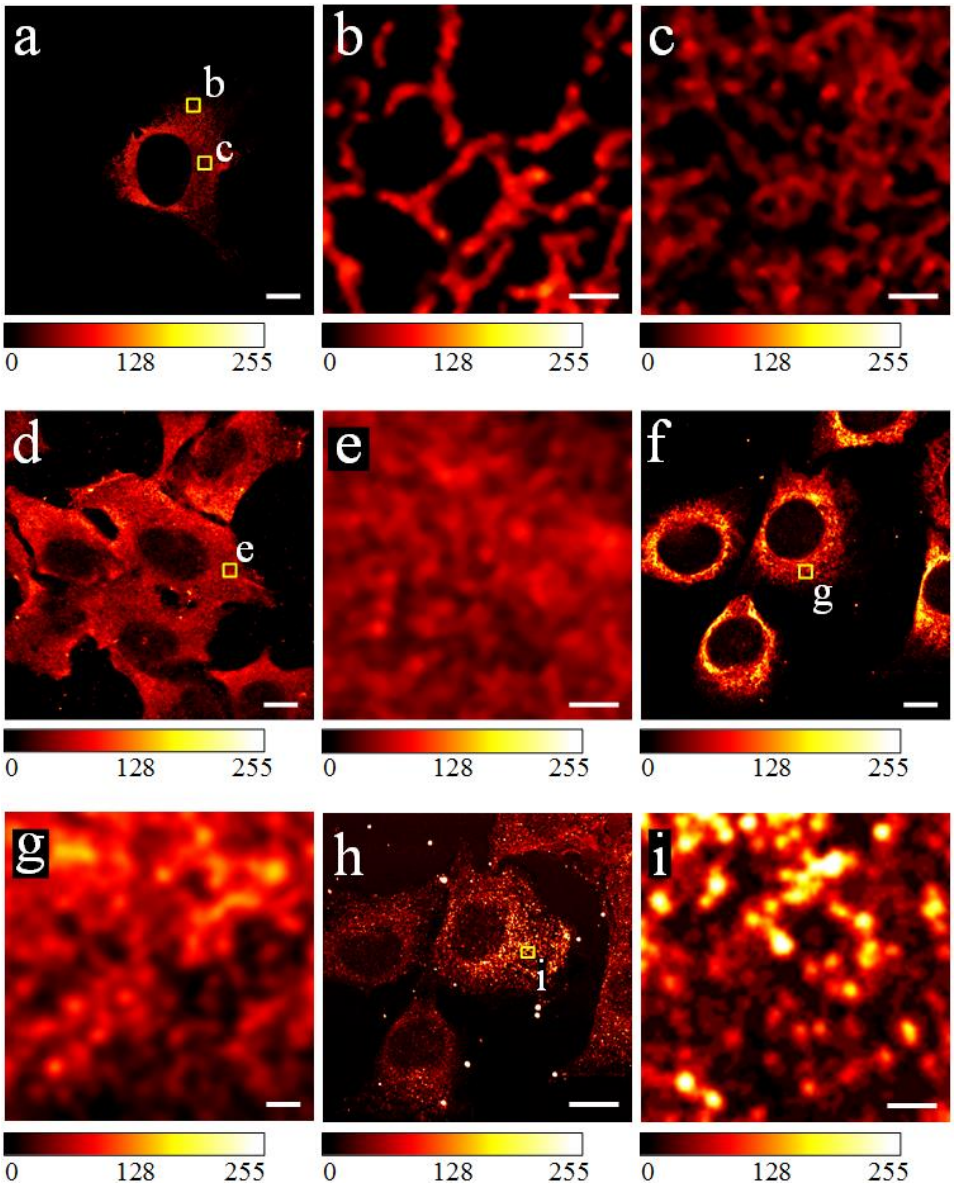

Figure 10: STED imaging of ER markers in C2C12 myoblasts

The STED images show representative examples of distinct ER markers in C2C12 myoblasts (day 2). **(a)**: By expressing KDEL-Crimson the ER/SR morphology of sheet-like domains connected by tubules was apparent. Scale bar: 10 µm. **(b)**: Tubules; inset from (a). Scale bar: 500 nm. **(c)**: Sheet-like domains; inset from (a). Scale bar: 500 nm. Alternative, previously established ER markers were used including Calreticulin, Sec61b and Nogo. **(d)**: The Calreticulin signal pattern (detected by rabbit anti-Calreticulin and anti-rabbit Abberior Star 635P) did not show the preference in sheets and tubules. Scale bar: 10 µm. **(e)**: Inset from (d). Scale bar: 500 nm. **(f)**: Sec61b signals did not clearly show the ER/SR domains (detected by rabbit anti-Sec61b and anti-rabbit Star635 P). Scale bar: 10 µm. **(g)**: Inset from (f). Scale bar: 500 nm. **(h)**: The Nogo signal pattern was punctate and did not show a clear preference for sheets and tubules (detected by goat anti-Nogo and anti-goat AlexaFluor 568). Scale bar: 10 µm. **(i)**: Inset from (h). Scale bar: 500 nm. The lookup table indicates the brightness by colour. For detailed information about antibody dilution, please refer to Materials and Methods (2.1.4).

3.3 Analysis of the subcellular distribution of V5-FL-JPH2 versus V5-ΔTM-JPH2 in HEK293a cells and C2C12 myoblasts

3.3.1 Area fraction of V5-JPH2 constructs

First, JPH2 signals were identified by image segmentation (Otsu Auto Threshold; see also Materials and Methods, 2.2.5.2). Consequently, the area fraction (see also 2.2.5.2) of the local JPH2 signal was measured for IF object signals per predefined ROI area as shown in Table 12. Furthermore, the number of objects per µm² was determined.

Table 11: Area fraction of JPH2 constructs in HEK293a cells and C2C12 myoblasts

Area fraction = object size ÷ ROI area	**Area fraction (%)**	**Number of ROIs**	**Number of clusters**	**Clusters per µm²**
V5-FL-JPH2 in HEK293a cells	11.6 ± 2,3*	5	11,011	4.7 ± 0.8**
V5-ΔTM-JPH2 in HEK293a cells	12.4 ± 2.6*	8	18,102	6.0 ± 0.8**
V5-FL-JPH2 in C2C12 myoblasts	5.0 ± 1.6#	12	14,761	3.4 ± 0.5##
V5-ΔTM-JPH2 in C2C12 myoblasts	9.7 ± 3.9#	8	9,629	3.6 ± 0.4##

* $p > 0.05$; # $p < 0.05$; ** $p < 0.05$; ## $p > 0.05$

In comparison with V5-FL-JPH2, the expression of the truncated V5-ΔTM-JPH2 led to a significantly larger ROI-normalised area fraction ($p < 0.05$; Table 12) in C2C12 myoblasts (day 2). This suggests that expression of V5-ΔTM-JPH2 in C2C12 myoblasts results in a global ER/SR distribution and further that the TM domain is not sufficient for local clustering of the V5-ΔTM-JPH2 protein. For V5-FL- versus V5-ΔTM-JPH2 in C2C12 myoblasts, there was no significant difference in the number of objects per µm² ($p > 0.05$; Table 12). In contrast, the area fraction of both constructs in HEK293a cells showed no significant difference ($p > 0.05$; Table 12). For HEK293a cells the expression of V5-ΔTM-JPH2 resulted in a significantly higher number of objects per µm² ($p > 0.05$ Table 12).

3.3.2 IF object size distribution

The object size distribution of V5-FL-JPH2 and V5-ΔTM-JPH2 was measured in HEK293a cells and C2C12 myoblasts (day 2) after Otsu Auto thresholding as shown in Figure 11.

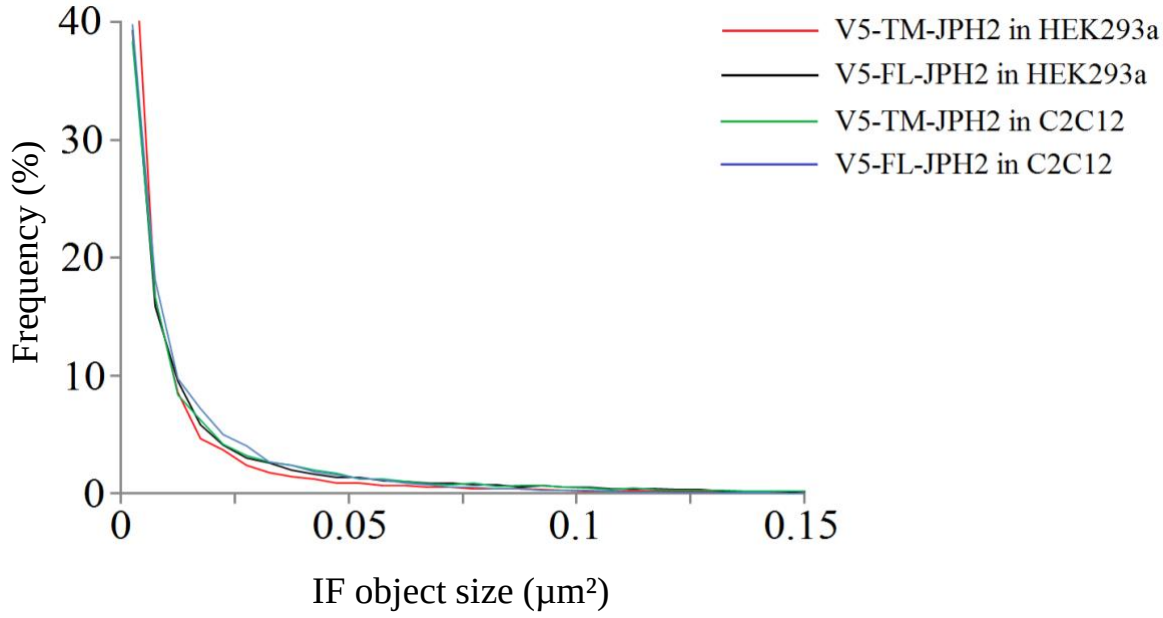

Figure 11: IF object size distribution in HEK293a cells and C2C12 myoblasts

The graph illustrates the measured IF object size distribution of V5-FL-JPH2 and V5-ΔTM-JPH2 in HEK293a and C2C12 myoblasts (day 2). The comparison between these expression constructs revealed no significant difference in the frequency of the signal size. Average ± SD is not shown for clarity. Number of Otsu-thresholded ROIs/cells: C2C12: 12 × V5-FL-JPH2, 8 × V5-ΔTM-JPH2; HEK293a cells: 5 × V5-FL-JPH2, 8 × V5-ΔTM-JPH2.

In summary, the data indicates a similar particle size distribution for V5-FL-JPH2 and V5-ΔTM-JPH2 each in HEK293a cells and C2C12 myoblasts (day 2), respectively. Accordingly, the frequency distribution throughout different object sizes is comparable between the two expression constructs.

3.3.3 Nearest neighbour distance (NND) analysis of V5-JPH2 signal peaks

To analyse the spatial relation between the local V5-JPH2 clusters, the signal peaks identified in STED images were analysed by the distance between the nearest neighbours (Figure 12).

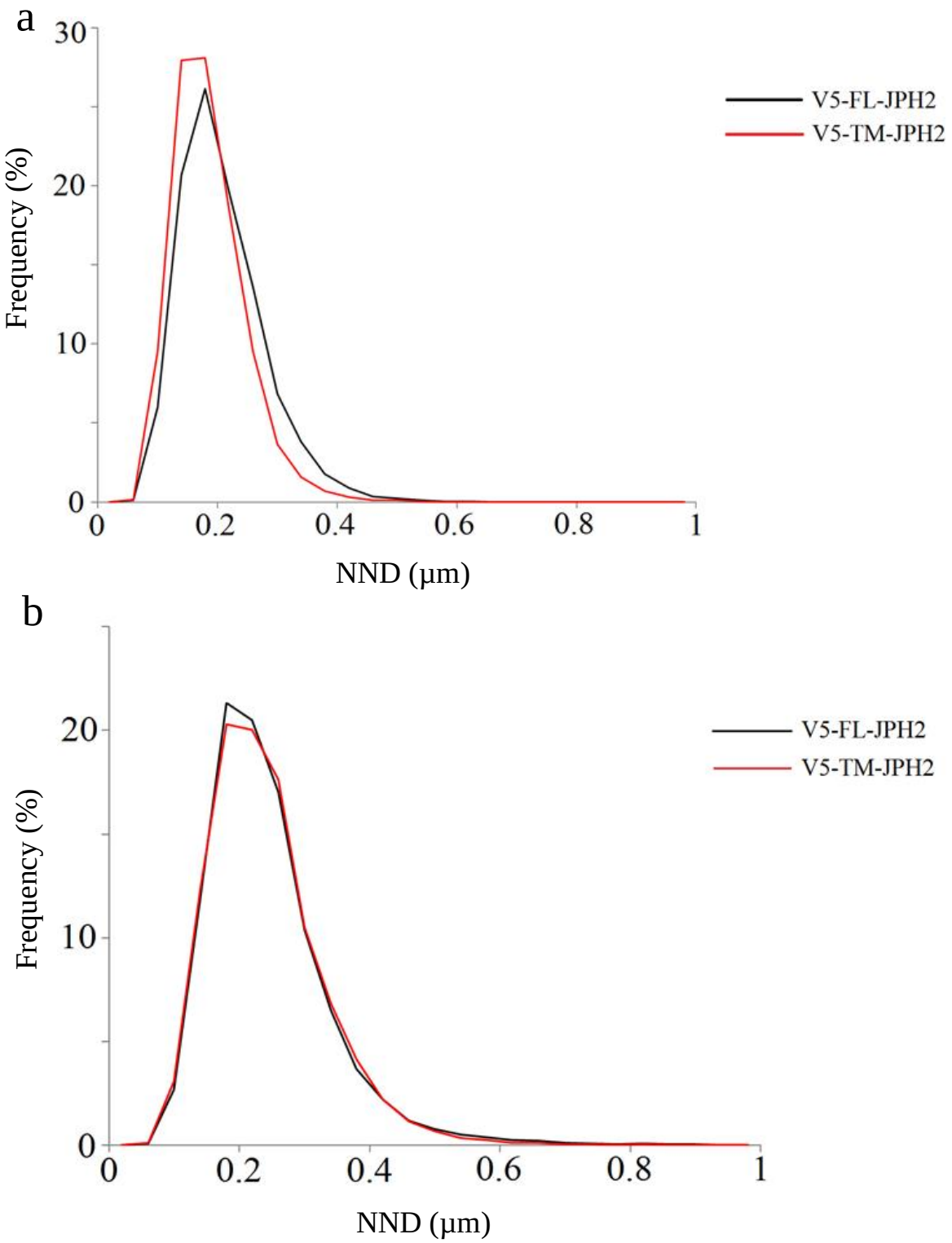

Figure 12: Frequency distribution of NND

The graphs illustrate the NND of V5-FL-JPH2 and V5-ΔTM-JPH2 in both **(a)**: HEK293a cells and **(b)**: C2C12 myoblasts (day 2). A signal peak was defined by an at least 10 grey scale units increased brightness. The comparison between V5-FL-JPH2 and V5-ΔTM-JPH2 in HEK293a cells and C2C12 myoblasts (day 2) showed no significant difference for the signal peak spacing (NND). Average ± SD is not shown for clarity. Number of Otsu thresholded ROIs/cells: C2C12: 12 × V5-FL-JPH2, 8 × V5-ΔTM-JPH2; HEK293a cells: 5 × V5-FL-JPH2, 8 × V5-ΔTM-JPH2.

In summary, the expression of V5-FL-JPH2 and V5-ΔTM-JPH2 in HEK293a cells and C2C12 myoblasts showed no significant difference for the frequency distribution of NND. This indicates a similar signal peak spacing within clusters for V5-FL-JPH2 and V5-ΔTM-JPH2, respectively.

3.3.4 Quantitative analysis of skeleton morphologies

In order to measure the spatial distribution of JPH2 constructs in ER structures, the geometry of spatially continuous V5-JPH2 signals was analysed. Therefore, following Otsu-thresholding, skeletons (see Materials and Methods, 2.2.5.5) were extracted from signal patterns to further analyse the distribution of skeleton lengths for V5-FL-JPH2 and V5-ΔTM-JPH2 in HEK293a cells and C2C12 myoblasts (Figure 13).

In C2C12 myoblasts the expression of V5-FL-JPH2 led to a significantly higher number of shorter skeleton components (284.9 ± 187.5 nm), whereas the expression of V5-ΔTM-JPH2 led to significantly longer skeleton components (329.0 ± 214.7 nm). In contrast, the mean skeleton length of V5-FL-JPH2 and V5-ΔTM-JPH2 expressed in HEK293a cells showed no significant difference ($p > 0.05$).

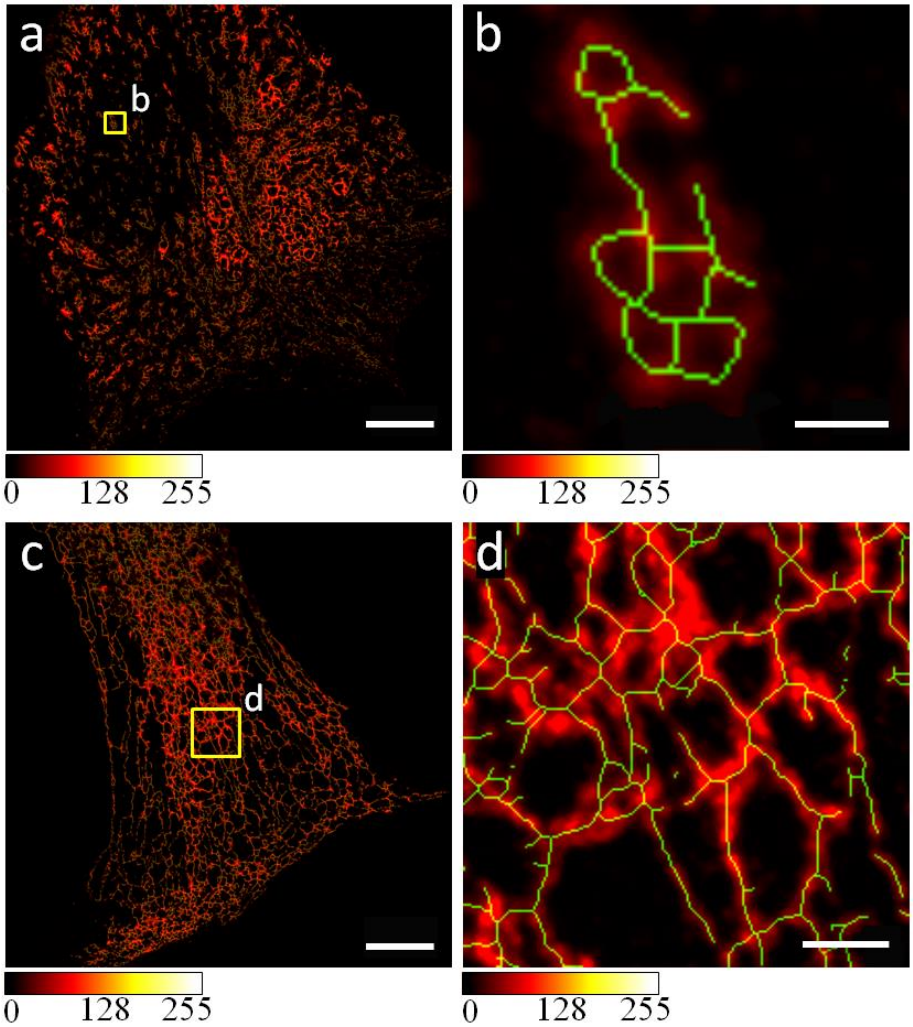

Figure 13: Overlay of representative STED images with skeleton data extracted by the "Skeletonize" plugin in Fiji

The morphology of V5-JPH2 products (detected by mouse anti-V5 and anti-mouse AlexaFluor 568) and their skeleton length was compared. For this, skeletons were extracted from Otsu thresholded ROIs by using the "Skeletonize" plugin of Fiji (see Materials and Methods, 2.2.5.5). The skeleton length distribution was then analysed to receive further insight into the different signal patterns of V5-FL-JPH2 and V5-ΔTM-JPH2. **(a)**: Overlay image of V5-FL-JPH2 expressed in a C2C12 myoblast (day 2) with skeleton data. Scale bar: 5 µm. **(b)**: Inset from (a). Scale bar: 200 nm. **(c)**: Overview image of truncated V5-ΔTM-JPH2 expressed in a C2C12 myoblast (day 2). Scale bar: 5 µm. **(d)**: Inset from (c). Scale bar: 500 nm. JPH2 signals are visualised in red, whereas skeletons are shown in green. The lookup table indicates the brightness rank of signals. For detailed information about antibody dilution, please refer to Materials and Methods (2.1.4).

The quantitative analysis of skeletons extracted from Otsu thresholded ROIs/cells revealed significant differences as shown in Figure 14.

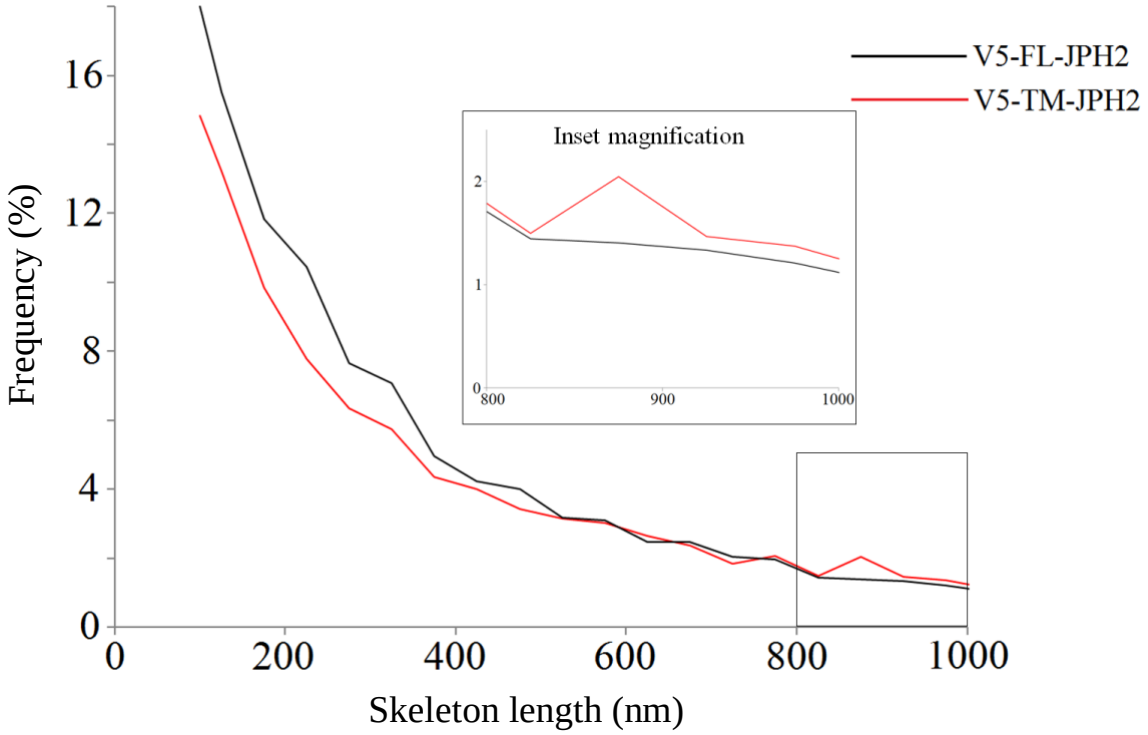

Figure 14: Skeleton length distribution of V5-JPH2 expression constructs in C2C12 myoblasts

Skeleton morphologies were analysed for total length of continuous branches. In particular, V5-ΔTM-JPH2 expression in C2C12 myoblasts (day 2) resulted in a higher number of longer skeletons (inset magnification), whereas V5-FL-JPH2 expression resulted in a higher number of shorter skeletons ($p < 0.05$). Skeletons close to the resolution limit were excluded for quantitative analysis. Skeletons larger than 1000 nm were excluded as low frequency outliers due to distorted mean values.

3.4 N-terminal truncation of V5-JPH2 leads to altered relations with RyR1 channels in C2C12 myotubes

Integrating differentiation and transfection protocols (see Materials and Methods, 2.2.1.6), C2C12 myotubes (day 7) were used to study the organisation and clustering of V5-JPH2 expression constructs during cell differentiation. In comparison to myoblasts, differentiated and multinucleated C2C12 myotubes express sufficient amounts of endogenous RyR1 channels to study their relation with JPH2 clusters. Dual-colour STED microscopy was used to visualise signal colocalisation with nanometric resolution. Different from myoblasts, myotubes show large dimensions up to 250 µm length and 20-30 µm thickness. Therefore, the myotube volume was imaged at two different depths: At the bottom, defining the first

layer of the resolvable signal (z = 0 µm) and further intracellular at ~2 µm depth to resolve the cellular cross-section of typical differentiated muscle cells (Figure 15).

3.4.1 V5-FL-JPH2 expression shows cluster generation in differentiated C2C12 myotubes

First, the signal distribution of endogenous JPH2 was visualised. Both, JPH2 signals near the PM/SL as well as a small number of longitudinally arranged JPH2 structures in the deeper section (z = 2µm) were detected. Subsequently, this signal pattern of V5-FL-JPH2 was compared with endogenous JPH2 concerning differences in intracellular localisation as well as the generation of JPH2 cluster structures.

Strikingly, the STED images indicated an overall similar distribution pattern for endogenous JPH2 and V5-FL-JPH2. Clustering of both, endogenous JPH2 as well as V5-FL-JPH2 was identified locally (Figure 15).

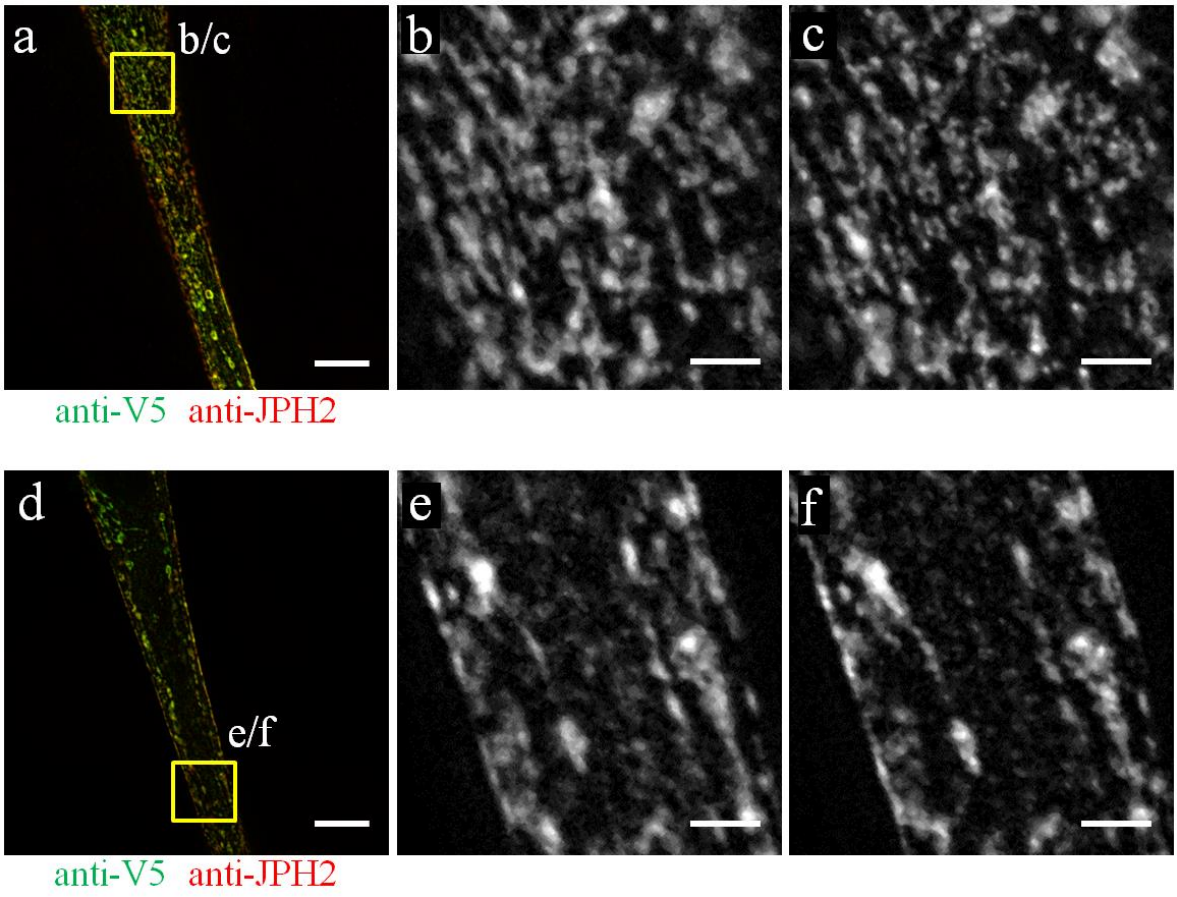

Figure 15: STED images of endogenous JPH2 and V5-FL-JPH2 in differentiated C2C12 myotubes

STED images show V5-FL-JPH2 (green) and endogenous JPH2 (red) in a C2C12 myotube (day 7) detected by mouse anti-V5 and anti-mouse AlexaFluor 568 as well as rabbit anti-JPH2 and anti-rabbit Star 635P. The dual-colour STED signal patterns of V5-FL-JPH2 and endogenous JPH2 were detected at the cell bottom and 2 µm further intracellular. **(a)**: STED image of spatially associated endogenous JPH2 and V5-FL-JPH2 at the cell bottom. Scale bar: 5 µm. **(b)**: Magnification of the V5-FL-JPH2 signal pattern; inset from (a). Scale bar: 1 µm. **(c)**: Magnification of the signal pattern of endogenous JPH2; inset from (a). Scale bar: 1 µm. **(d)**: Longitudinally oriented cluster structures of endogenous JPH2 and V5-FL-JPH2 were apparent in the deeper section (2 µm). Scale bar: 5 µm. **(e)**: V5-FL-JPH2 signal pattern in the deeper section (2 µm); inset from (d). Scale bar: 1 µm. **(f)**: Endogenous JPH2 clusters in the deeper section (2 µm). Scale bar: 1 µm. For detailed information about antibody dilution, please refer to Materials and Methods (2.1.4).

To relate the JPH2 signal to a previously identified interaction partner, dual-colour STED of V5-FL-JPH2 and RyR1 channels was performed. First, colocalisation of endogenous JPH2 with RyR1 channels was confirmed (Figure 16). The signals were detected locally and showed a spatial association. JPH2 signal from clusters was predominantly detected near the PM/SL in larger domains of the SR, whereas a small number of longitudinal orientated signals at the cell centre was also visualised. Subsequently, the RyR1 and V5-FL-JPH2

signals were compared (Figure 16). Similar to endogenous JPH2, V5-FL-JPH2 was spatially associated with RyR1 channels in the same SR sub-domains.

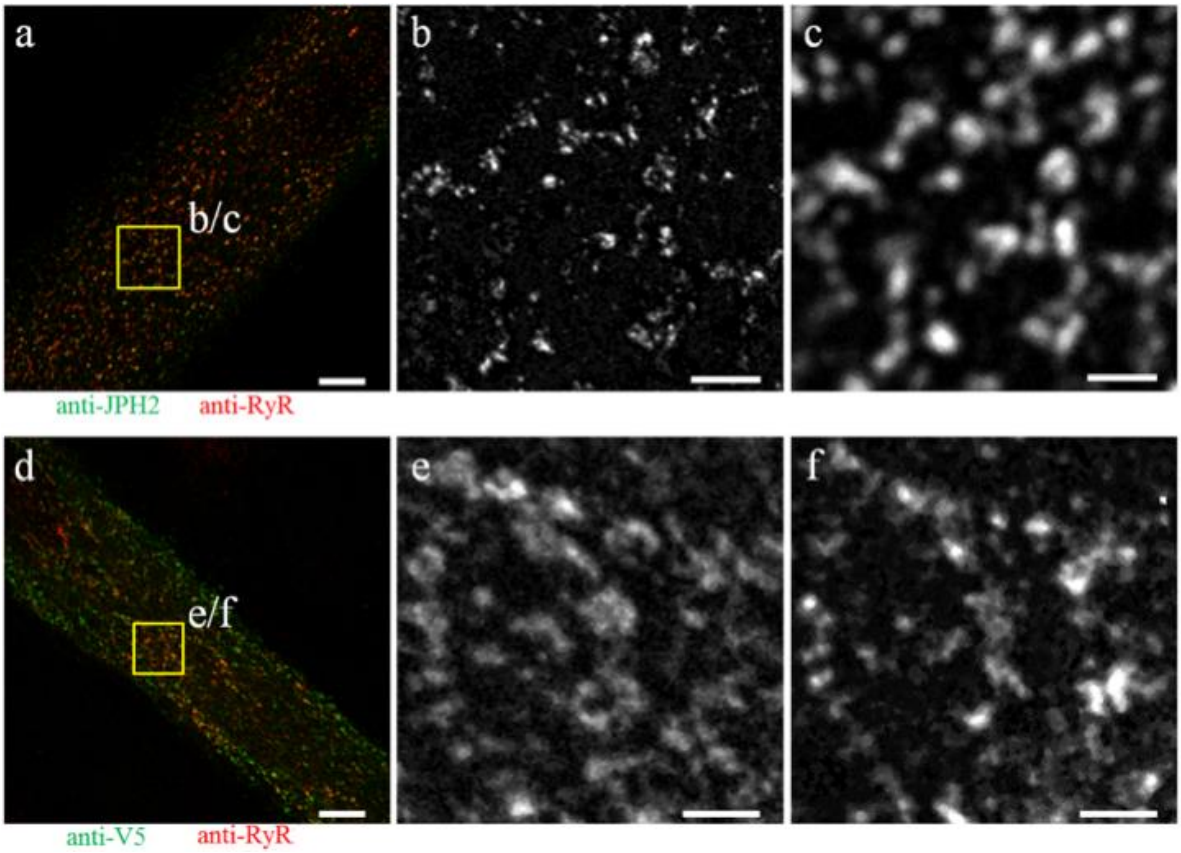

Figure 16: STED images of endogenous JPH2, V5-FL-JPH2 and RyR1 channels in differentiated C2C12 myotubes

The STED images show the spatial association between endogenous JPH2 and RyR1 channels (detected by rabbit anti-JPH2 and anti-rabbit Star 635P; mouse anti-RyR and anti-mouse AlexaFluor 568) as well as V5-FL-JPH2 and RyR1 channels (detected by rabbit anti-V5 and anti-rabbit Star 635 P; mouse anti-RyR and anti-mouse AlexaFluor 568) in C2C12 myotubes (day 7). **(a)**: Endogenous JPH2 (green) built clustered structures that were spatially associated with RyR1 clusters (red). Scale bar: 5 µm. **(b)**: Signal pattern of endogenous JPH2; inset from (a). Scale bar: 500 nm. **(c)**: Signal pattern of RyR1 channels; inset from (a). Scale bar: 500 nm. **(d)**: Expression of V5-FL-JPH2 (green) in C2C12 myotubes (day 7) resulted in clustered structures that were spatially associated with RyR1 clusters at the myotube centre (red). Scale bar: 5 µm. **(e)**: Signal pattern of V5-FL-JPH2; inset from (d). Scale bar: 500 nm. **(f)**: Signal pattern of RyR1 channels; inset from (d). Scale bar: 500 nm. For detailed information about antibody dilution, please refer to Materials and Methods (2.1.4).

As expected, within individual clusters, superresolution STED microscopy showed interspersed signal peaks related to V5-FL-JPH2 and RyR1 channels (Figure 17).

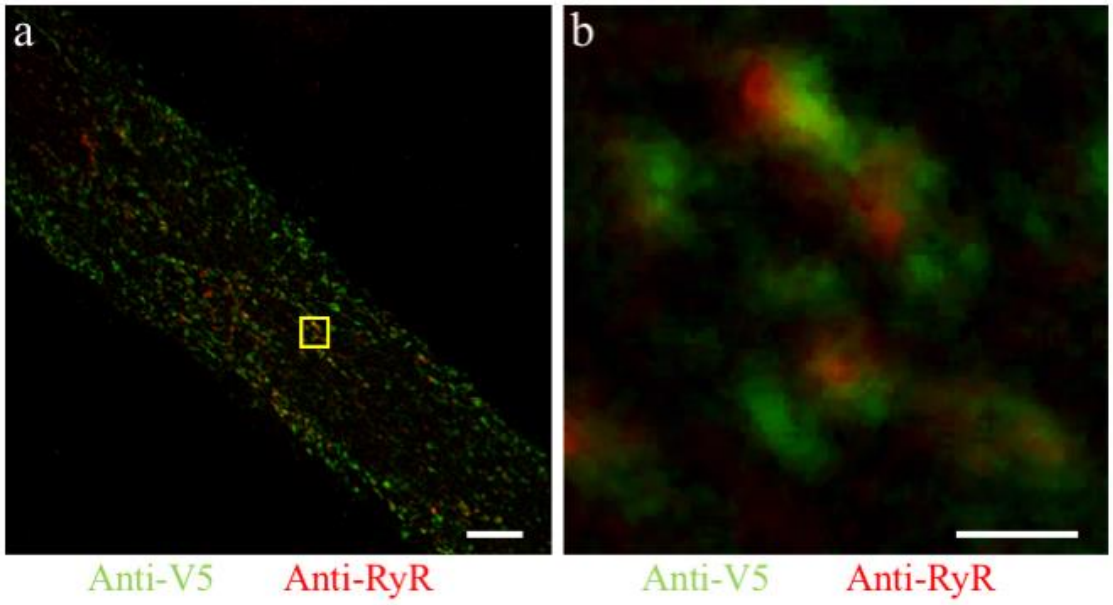

Figure 17: Spatial relation of V5-FL-JPH2 and RyR1 channels in a C2C12 myotube (day 7)

(a): STED image of recombinant V5-FL-JPH2 (green; detected by rabbit anti-V5 and anti-rabbit Star 635P) and endogenous RyR1 channels (red; detected by mouse anti-RyR and anti-mouse AlexaFluor 568) in a C2C12 myotube (day 7). Scale bar: 5 µm. **(b)**: Inset from (a). In cluster areas V5-FL-JPH2 and RyR1 signals mostly interspersed and sometimes colocalised. Scale bar: 500 nm. For detailed information about antibody dilution, please refer to Materials and Methods (2.1.4).

Multinucleated C2C12 myotubes at an early state of maturation (day 5) did not express sufficient levels of endogenous RyR1 channels for IF detection. Strikingly, expression of V5-FL-JPH2 in these C2C12 myotubes (day 4) still resulted in clustered structures (Figure 18).

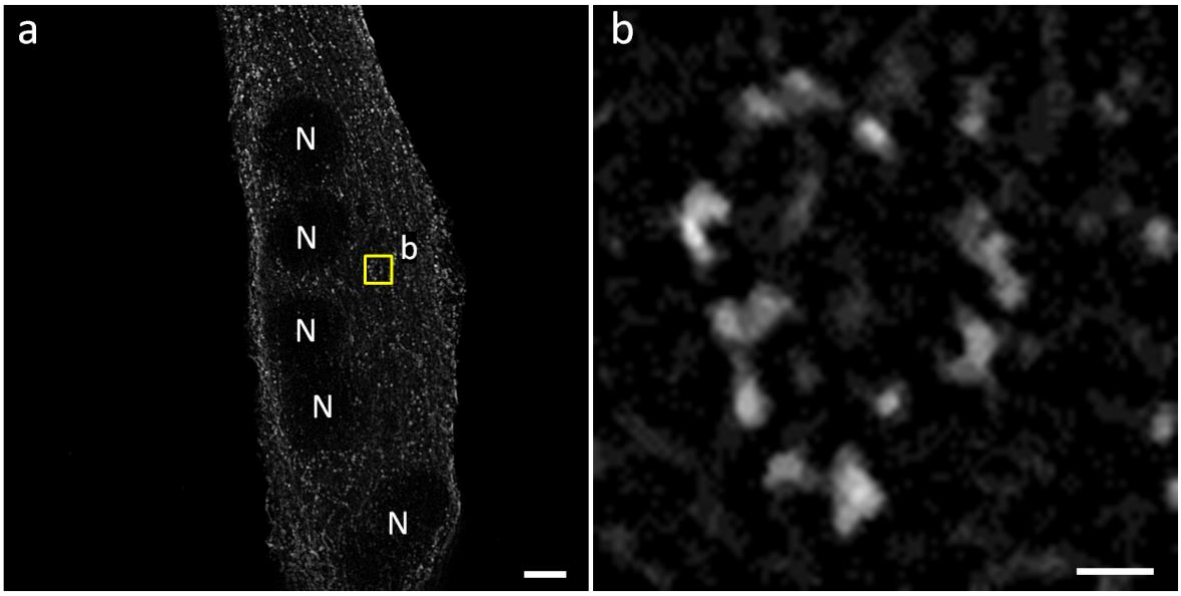

Figure 18: STED imaging of V5-FL-JPH2 in a C2C12 myotube (day 5)

(a): The STED image shows V5-FL-JPH2 signals in a multinucleated C2C12 myotube at an early state of maturation (day 4) detected by rabbit anti-V5 and anti-rabbit Star 635P. At this stage, the C2C12 myotube did not express a sufficient level of RyR1 channels for IF detection. Notably, V5-FL-JPH2 expression resulted in clustered structures. N: Nucleus; Scale bar: 5 µm. **(b)**: Clustered V5-FL-JPH2 signals; inset from a. Scale bar: 500 nm. For detailed information about antibody dilution, please refer to Materials and Methods (2.1.4).

3.4.2 V5-ΔTM-JPH2 signal association with endogenous JPH2 and RyR2 channels in C2C12 myotubes

Using STED microscopy the spatial relation between V5-ΔTM-JPH2 and endogenous JPH2 was visualised. Furthermore, the spatial association between V5-ΔTM-JPH2 and endogenous RyR1 channels was investigated.

There was no systematic overlap between the V5-TΔM-JPH2 signal and endogenous JPH2 (Figure 19). In contrast to clusters of endogenously expressed JPH2, V5-ΔTM-JPH2 signals occurred throughout tubular and reticular structures and were distributed ubiquitously throughout the SR network components.

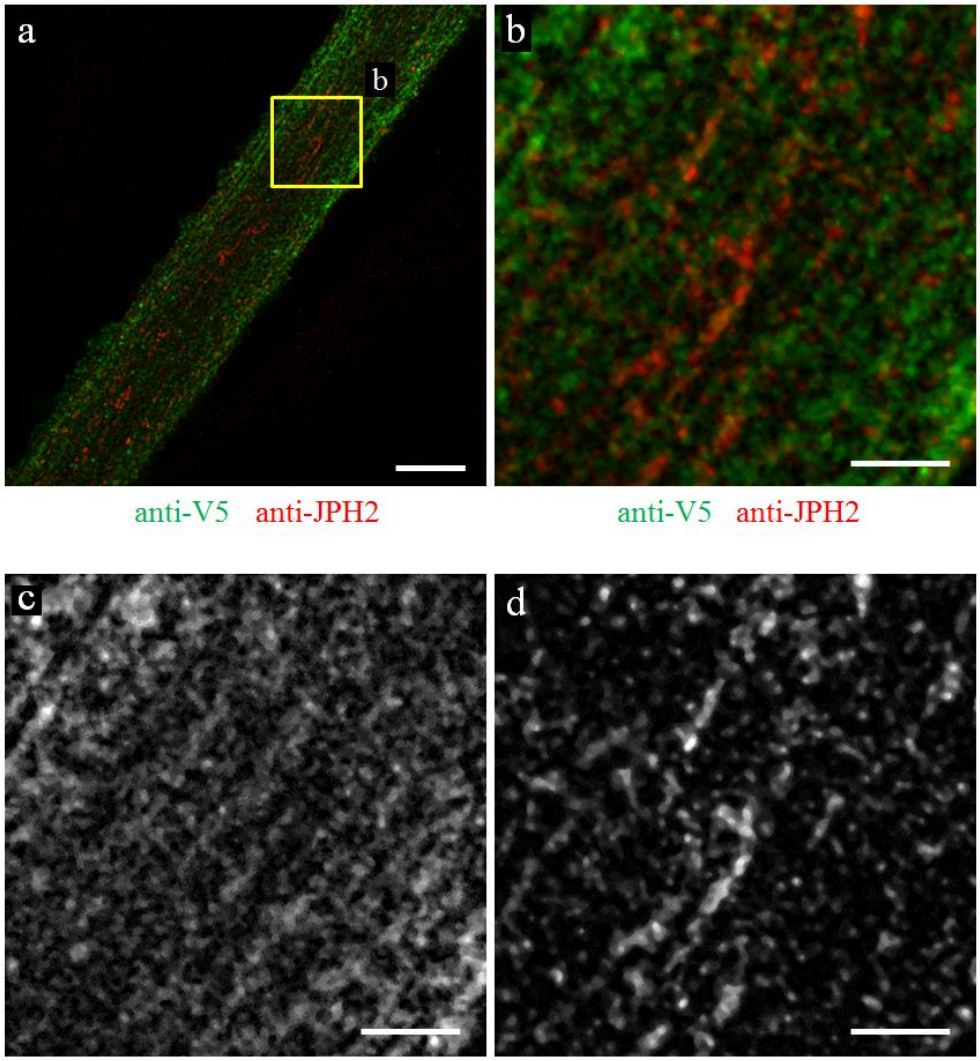

Figure 19: STED imaging of endogenous JPH2 and V5-ΔTM-JPH2 in a C2C12 myotube

The signals of endogenous JPH2 (red) and the truncated V5-ΔTM-JPH2 expression construct (green) showed no systematic association in C2C12 myotubes (day 7). Endogenously expressed JPH2 built clustered signal structures, whereas V5-ΔTM-JPH2 expression resulted in ubiquitous distribution throughout the SR. **(a)**: STED image of endogenous JPH2 (detected by rabbit anti-JPH2 and anti-rabbit Star 635P) and V5-ΔTM-JPH2 (detected by mouse-anti-V5 and anti-mouse AlexaFluor 568) in a C2C12 myotube (day 7). Scale bar: 5 µm. **(b)**: Inset from (a). Scale bar: 1 µm. **(c)**: Reticular V5-ΔTM-JPH2 signal pattern from (b). Scale bar: 1 µm. **(d)**: Signal pattern of endogenous JPH2 from (b). Scale bar: 1 µm. For detailed information about antibody dilution, please refer to Materials and Methods (2.1.4).

Subsequently, spatial associations between V5-ΔTM-JPH2 and endogenous RyR1 channels were visualised. In contrast to V5-FL-JPH2, the expression of V5-ΔTM-JPH2 did not lead to a specific association with RyR1 clusters (Figure 20).

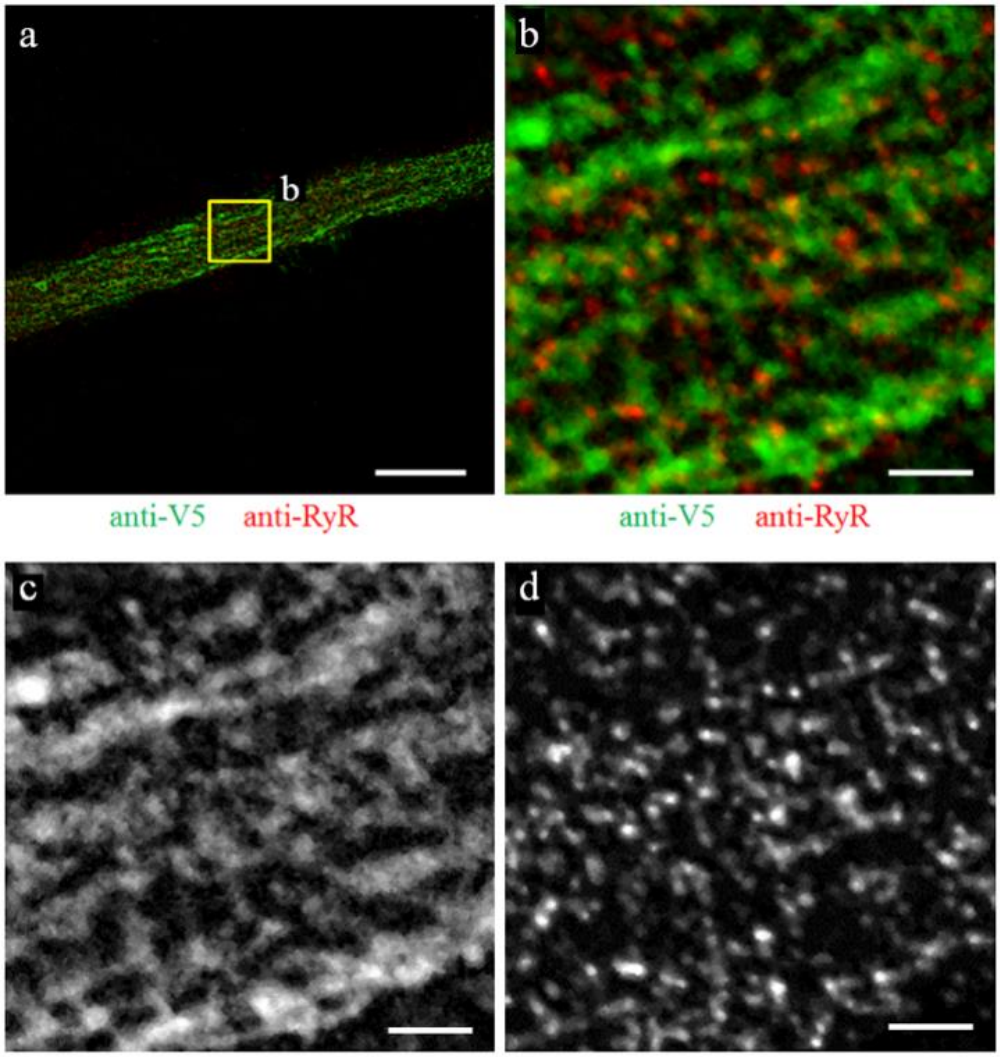

Figure 20: STED imaging of V5-ΔTM-JPH2 and RyR1 IF-signals in a C2C12 myotube (day 7)

Expression of V5-ΔTM-JPH2 (green) in C2C12 myotubes (day 7) showed no locally restricted RyR1 (red) association. V5-ΔTM-JPH2 signals (detected by rabbit anti-V5 and anti-rabbit Star 635P) were distributed in reticular structures and ubiquitously throughout the SR network, whereas RyR1 channels (detected by mouse anti-RyR and anti-mouse AlexaFluor 568) formed distinct clusters. **(a)**: STED image of V5-ΔTM-JPH2 expression construct and RyR1 channels in a C2C12 myotube (day 7). Scale bar: 5 µm. **(b)**: Inset from (a). Scale bar: 1 µm. **(c)**: Reticular V5-ΔTM-JPH2 signal pattern from b. Scale bar: 1 µm. **(d)**: Clustered signal pattern of RyR1 channels from b. Scale bar: 1 µm. For detailed information about antibody dilution, please refer to Materials and Methods (2.1.4).

3.5 V5-FL-JPH2 and V5-ΔDR-TM-JPH2 clustering in neonatal rat cadiomyocytes

NRCM (see Materials and Methods, 2.1.7) were used to investigate the subcellular localisation and clustering of V5-FL-JPH2, V5-ΔDR-TM-JPH2 and V5-ΔTM-JPH2 in a

cardiac cell system. V5-FL-JPH2 was compared to a TM only deletion construct (V5-ΔTM-JPH2). Here, the approach was extended to V5-ΔDR-TM-JPH2, which includes the cytosolic divergent region (DR) continuous with the TM domain, while the α-helix and the MORN-motifs are deleted. Following transfection, subcellular signals were correlated to the endogenous RyR2 signal to elucidate the potential for local interactions in the cardiac NRCM cell model.

Similar to the myotube images, expression of V5-FL-JPH2 resulted in cluster-like signal morphologies. Moreover, V5-FL-JPH2 signals were spatially associated with the endogenous RyR2 cluster signals (Figure 21a and 21b). In contrast, the V5-ΔTM-JPH2 signal pattern was more ubiquitously distributed throughout the SR network. A spatial association with RyR2 channels in the same SR sub-domains was not detectable (Figure 21c and 21d).

Similar to V5-FL-JPH2, the expression of V5-ΔDR-TM-JPH2 in NRCM revealed signal patches closely associated with endogenous RyR2 cluster signals (Figure 21e and 21f). This indicates a similar signal association between V5-FL-JPH2 and V5-ΔDR-TM-JPH2 with RyR2 channels. The signals of recombinant V5-FL-JPH2 and V5-ΔDR-TM-JPH2 did not perfectly overlap with endogenous RyR2 signals but mostly interspersed throughout the cluster area.

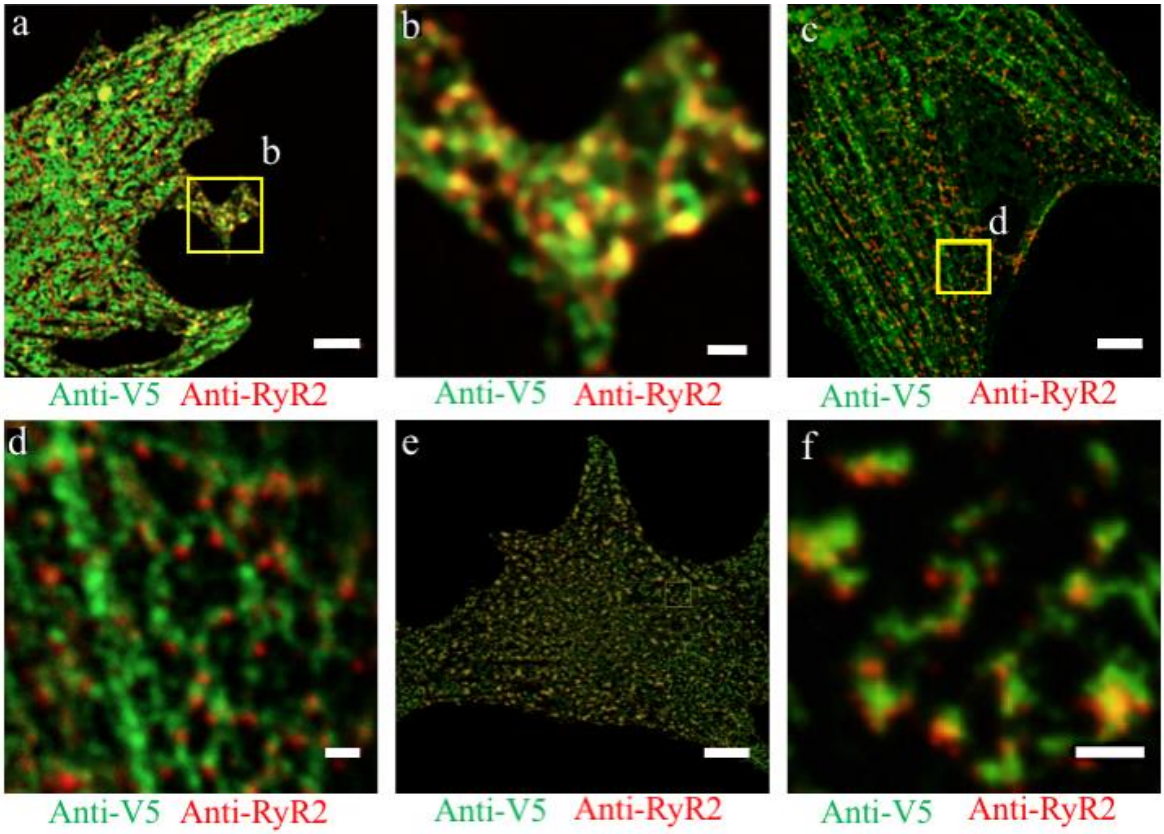

Figure 21: STED images of V5-FL-JPH2, V5-ΔDR-TM-JPH2 and V5-ΔTM-JPH2 in NRCM

The STED images visualise the spatial relation of recombinant JPH2 (green; detected by rabbit anti-V5 and anti-rabbit Star 635P) and endogenous RyR2 (red; detected by mouse anti-RyR2 and anti-mouse AlexaFluor 568). **(a)**: STED image of the V5-FL-JPH2 expression construct and RyR2 channels in NRCM. Scale bar: 5 µm. **(b)**: Inset from (a). The image shows a spatial association between V5-FL-JPH2 and RyR2 signals. Scale bar: 500 nm. **(c)**: STED overview image of the V5-ΔTM-JPH2 construct and RyR2 channels in NRCM. Scale bar: 5 µm. **(d)**: Inset from (c). The V5-ΔTM-JPH2 signals were distributed ubiquitously throughout the SR with a reticular and tubular signal pattern, whereas RyR2 signals showed cluster-like formations. Scale bar: 500 nm. **(e)**: STED image of N-terminally truncated V5-ΔDR-TM-JPH2 and RyR2 channels in NRCM. Scale bar: 5 µm. **(f)**: Inset from (e). The expression of V5-ΔDR-TM-JPH2 in NRCM led to clustered signals in close spatial proximity to RyR2 clusters. Scale bar: 500 nm. The signals of both, V5-FL-JPH2 and V5-ΔDR-TM-JPH2, did not perfectly overlap with RyR2 signals but interspersed within a cluster area. For detailed information about antibody dilution, please refer to Materials and Methods (2.1.4).

The signal pattern of the recombinant JPH2 constructs was quantified to characterise their SR distribution. Image segmentation of the cluster objects was accomplished by Otsu thresholding (see Materials and Methods, 2.2.5.2). Subsequently, the cluster area, the signal area fraction and the circularity of clusters was analysed.

The cluster area was significantly different between the different recombinant JPH2 expression constructs (Figure 22a). Interestingly, the mean cluster area was significantly

smaller for V5-FL-JPH2 and V5-ΔDR-TM-JPH2. In contrast, the V5-ΔTM-JPH2 signal pattern showed a largely scattered distribution and ~4-fold larger average cluster size (Table 13). In accordance with this finding, V5-FL-JPH2 and V5-ΔDR-TM-JPH2 signals showed a more circular shape than V5-ΔTM-JPH2 (Figure 22c). This result is in line with a more reticular and thus elongated distribution for V5-ΔTM-JPH2 clusters in analogy to the results in C2C12 cells.

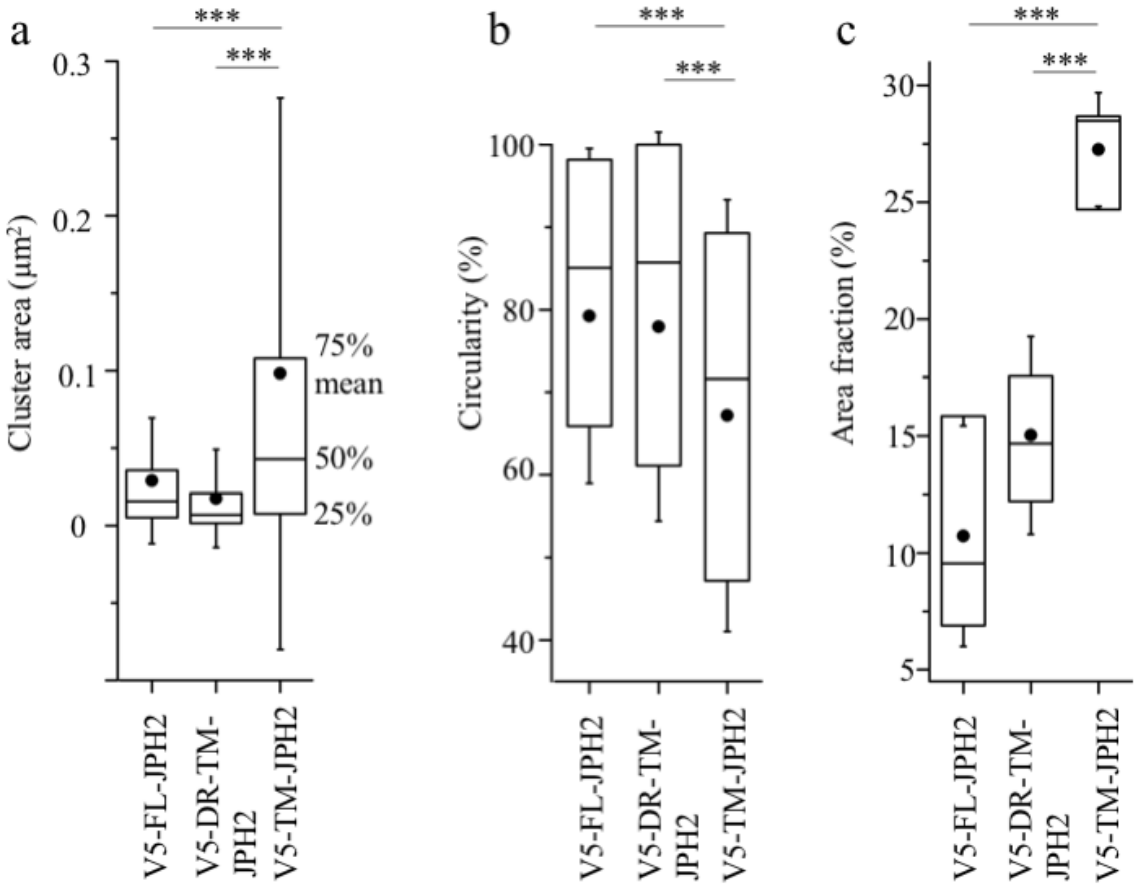

Figure 22: Cluster area, area fraction and circularity of V5-FL-JPH2, V5-ΔDR-TM-JPH2 and V5-ΔTM-JPH2 in NRCM

Boxplots displaying cluster area, circularity and area fraction of recombinant V5-JPH2 constructs in NRCM. **(a)**: In contrast to V5-FL-JPH2 and V5-ΔDR-TM-JPH2, V5-ΔTM-JPH2 signals distributed to significantly larger structures ($p < 0.05$). **(b)**: V5-FL-JPH2 and V5-ΔDR-TM-JPH2 were organised in more circular structures, whereas the circularity of V5-TΔM-JPH2 structures was significantly lower ($p < 0.05$). **(c)**: The ratio of defined objects per area (area fraction) was significantly higher for V5-ΔTM-JPH2 ($p < 0.05$). Consequently, image analysis indicated that V5-ΔDR-TM-JPH2 signal distribution was more similar to the V5-FL-JPH2 phenotype than V5-ΔTM-JPH2 and that this difference was functionally connected to the divergent region present in V5-ΔDR-TM-JPH2 but not V5-ΔTM-JPH2. *** Mann-Whitney test with Bonferroni correction: $p < 0.05$.

The numbers in Table 12 show the mean values of cluster area, area fraction and circularity analysis in NRCM.

Table 12: Cluster area, area fraction and circularity of V5-FL-JPH2, V5-ΔDR-TM-JPH2 and V5-ΔTM-JPH2 in NRCM

	V5-FL-JPH2	V5-ΔDR-TM-JPH2	V5-ΔTM-JPH2
Number of cells	7	6	6
Number of clusters	10,707	11,866	5,639
Cluster area (µm²)	0.03 ± 0.04	0.02 ± 0.03	0.99 ± 0.17*
Clusters per µm²	3.6 ± 0.4	9.4 ± 1.5*	2.8 ± 0.4*
Area fraction (%)	10.7 ± 4.7	15.0 ± 4.2	27.3 ± 2.4*
Circularity (%)	79 ± 20	78 ± 20	67 ± 30*

* Mann-Whitney test with Bonferroni correction: $p < 0.05$ versus V5-FL-JPH2

3.6 Mutations that change the intracellular localisation of His6-tagged recombinant JPH2 constructs

The way recombinant JPH2 was kept in the ER/SR was investigated by inserting distinct mutations into the TM domain of His6-ΔTM-JPH2 (Materials and Methods, 2.1.6.2). Here, the expression constructs included a N-terminal His6-tag for indirect IF labelling. The design of the C-terminal mutations in the TM domain was based on information from the literature (Materials and Methods, 2.1.6.2). The experiments included the expression of His6-ΔTM-JPH2-C678A, His6-ΔTM-JPH2-C678A-N684L, His6-ΔTM-JPH2-N684L, His6-FL-JPH2-4L and His6-FL-JPH2-8L in HEK293a cells as well as in C2C12 myoblasts.

3.6.1 Impact of the C678A and the N684L mutation on the intracellular His6-ΔTM-JPH2 signal localisation

The signal pattern of His6-ΔTM-JPH2-C678A, His6-ΔTM-JPH2-C678A-N684L and His6-ΔTM-JPH2-N684L was compared to the control construct (His6-ΔTM-JPH2).

Similar to the control (Figure 23a), the expression of His6-ΔTM-JPH2-C678A (Figure23b) and His6-ΔTM-JPH2-C678A-N684L (Figure 23c) in HEK293a cells resulted in a reticular ER and perinuclear signal pattern. Therefore, no evidence for an intracellular relocation was

found. In contrast, the expression of His6-ΔTM-JPH2-N684L resulted in a strong nuclear signal (Figure 23d). Additionally, similar results were confirmed in C2C12 myoblasts (data not shown).

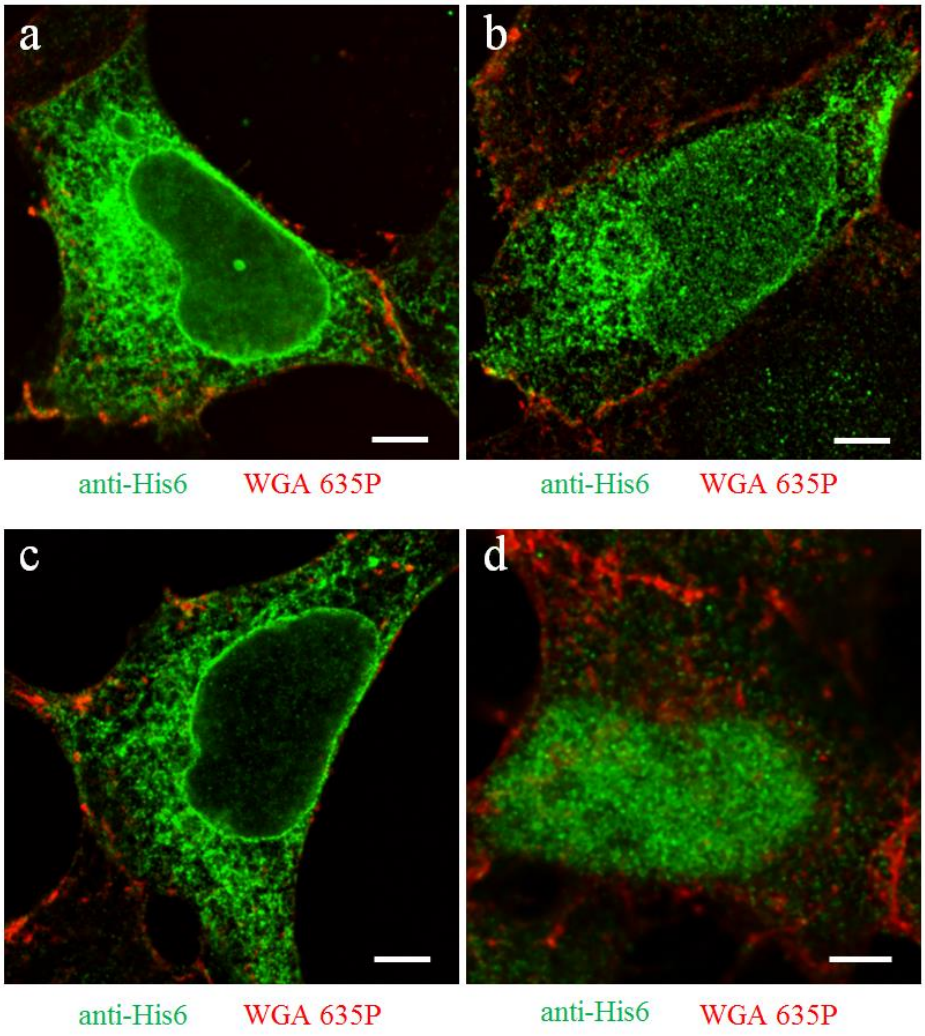

Figure 23: Confocal images of His6-ΔTM-JPH2 expression constructs in HEK293a cells

Confocal images showing representative examples of different His6-TM-JPH2 expression constructs (green) in HEK293a cells (detected by mouse anti-His6 and anti-mouse AlexaFluor 568). The PM is labelled with WGA 635P (red). Similar to the signal pattern of non-mutated His6-ΔTM-JPH2, the expression of His6-TΔM-JPH2-C678A and His6-ΔTM-JPH2-C678A-N684L resulted in a reticular signal appearance. In contrast, the expression of His6-ΔTM-JPH2-N684L led to a strong nuclear signal. **(a)**: His6-ΔTM-JPH2 (control). Scale bar: 5 µm. **(b)**: His6-FL-JPH2-C678A. Scale bar: 5 µm. **(c)**: His6-ΔTM-JPH2-C678A-N684L. Scale bar: 5 µm. **(d)**: His6-TΔM-JPH2-N684L. Scale bar: 5 µm. For detailed information about antibody dilution, please refer to Materials and Methods (2.1.4 and 2.1.5).

A possible mutation-dependent relocation of His6-TM-JPH2 to the ER-Golgi intermediate compartment (ERGIC) was investigated. For this, the His6-ΔTM-JPH2 mutants were co-labelled with a specific ERGIC marker (ERGIC-53; see also Materials and Methods, 2.1.4.1).

However, STED imaging did not support colocalisation of His6-ΔTM-JPH2-C678A-N684L (Figure 24 a and b), His6-ΔTM-JPH2-C678A (not shown) and His6-ΔTM-JPH2-N684L (not shown) with ERGIC-53. Moreover, line profiles indicated a spatial gap arrangement (Figure 24 c) supporting a juxtaposition of His6-ΔTM-JPH2 containing ER domains and ERGIC-53.

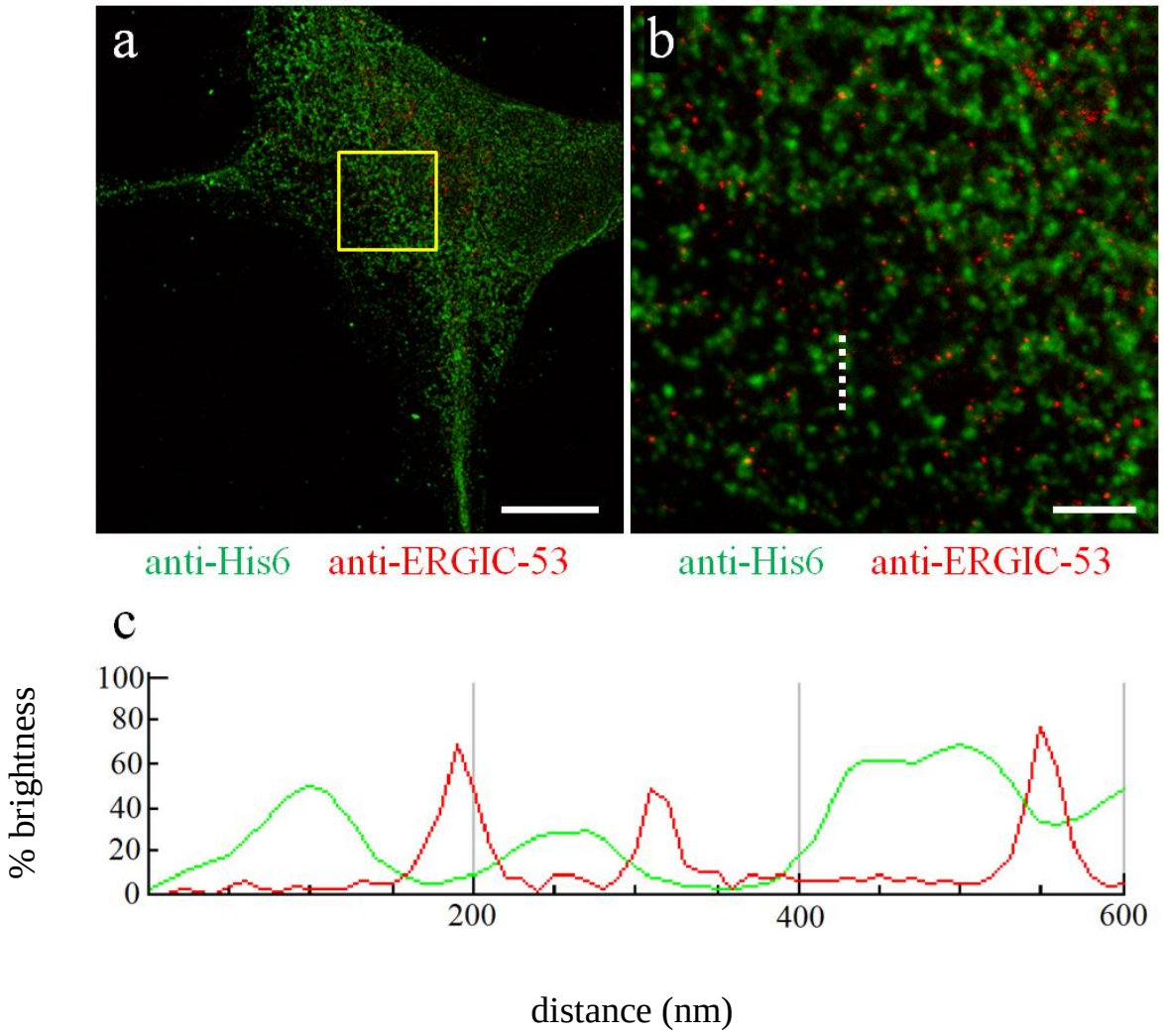

Figure 24: STED image of His6-ΔTM-JPH2-C678A-N684L and ERGIC-53 in HEK293a cell

(a): The overview image shows a representative example of His6-ΔTM-JPH2-C678A-N684L (green; detected by mouse anti-His6 and anti-mouse AlexaFluor 568) expressed in a HEK293a cell co-labelled with ERGIC-53 (red; detected by rabbit anti-ERGIC-53 and anti-rabbit Star 635P). Scale bar: 5 µm. **(b)**: Magnification of (a) showing the gap arrangement of His6-ΔTM-JPH2-C678A-N684L and ERGIC-53. This gap arrangement was confirmed by line profiles (dotted line). Scale bar: 1 µm. **(c)**: Line profile of dotted line in (c). The result confirms a spatial separation between His6-ΔTM-JPH2-C678A-N684L and ERGIC-53 signals.

3.6.2 Impact of a C-terminal 4L/8L extension on the intracellular localisation of His6-FL-JPH2

The TM domain of the His6-FL-JPH2 expression construct was extended by 4 or 8 additional leucine residues (Materials and Methods, 2.1.6.2) to investigate potential changes in ER/SR domains and a potential relocation to the PM/SL. These recombinant expression constructs

were expressed both in HEK293a cells and C2C12 myoblasts (not shown) and each compared to the control (His6-FL-JPH2).

In contrast to the control (Figure 25a), which resulted in the expected clustered signal appearance, the extended His6-FL-JPH2-4L and His6-FL-JPH2-8L constructs showed a nuclear signal retention (Figure 25b and c). There was no evidence for relocation of the 4L/8L extended His6-FL-JPH2 constructs to the PM/SL.

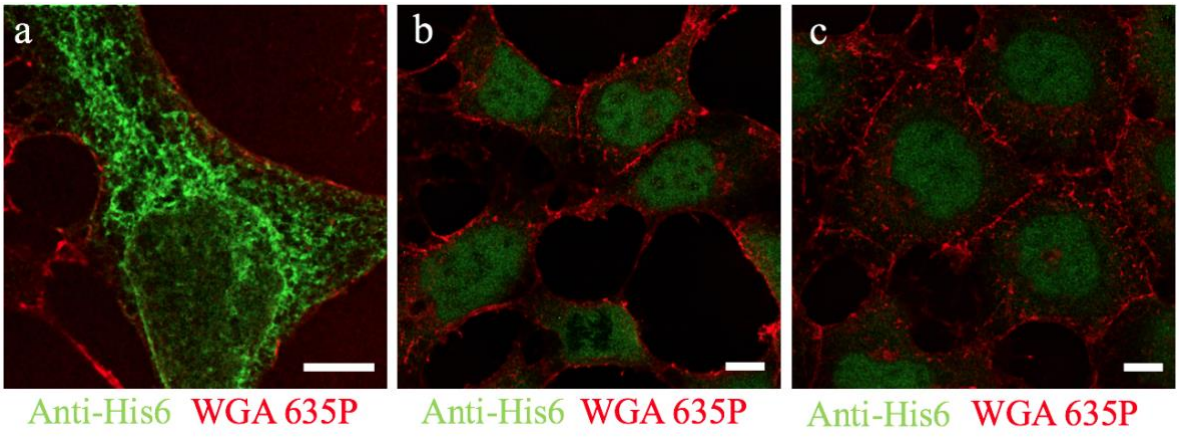

Figure 25: Confocal images of 4L/8L-extended His6-FL-JPH2 in HEK293a cells

(a): The expression of His6-FL-JPH2 (green) in a HEK293a cell resulted in a reticular signal pattern. The plasma membrane is visualised in red. **(b)**: In contrast, the expression of His6-FL-JPH2 extended by 4 leucine residues (4L) showed a diffuse nuclear signal. **(c)**: Similar to the results from (b) the expression of the C-terminal 8L extension of His-FL-JPH2 resulted in a diffuse nuclear signal. Scale bars: 5 µm. His6-FL-JPH2 signals were detected by mouse anti-His6 and anti-mouse AlexaFluor 568. The PM was stained with WGA635P. For detailed information about antibody dilution, please refer to Materials and Methods (2.1.4 and 2.1.5).

5. Discussion

5.1 Brief summary of the results

Superresolution STED microscopy was used to elucidate the intracellular spatial distribution of recombinant V5-JPH2 proteins in HEK293a, C2C12 and NRCM cells in order to gain insight into specific clustering behaviours of JPH2 domains. By applying quantitative analysis strategies, significant differences between distinct V5-FL-JPH2, V5-ΔDR-TM-JPH2 and V5-ΔTM-JPH2 products were detectable through altered ER/SR signal distributions. In this context, subcellular ER/SR organisation of different recombinant V5-JPH2 proteins depended further on the cell type as well as cell-specific maturity. ER/SR localisation was confirmed by correlating the signal of recombinant V5-JPH2 proteins with KDEL-Crimson.

First, in NRCM expression of V5-FL-JPH2 typically resulted in clustered signal areas that were spatially associated with RyR2 cluster signals. Moreover, the V5-FL-JPH2 signal pattern was similar to endogenous JPH2 cluster signals. In contrast, expression of V5-ΔTM-JPH2 led to a more ubiquitous ER/SR protein distribution apparent as a continuous reticular signal pattern. Interestingly, V5-ΔDR-TM-JPH2 also showed clustered signals again in close spatial proximity with RyR2 cluster signals. Besides the spatial relation with RyR2 clusters quantitative signal analysis revealed that V5-FL-JPH2 and V5-ΔDR-TM-JPH2 occurred in a large number of smaller signal objects with a high circularity clearly in contrast with V5-ΔTM-JPH2 that lost the ability for clustering in ER/SR domains.

Second, in mature C2C12 myotubes (day 7), which express endogenous RyR1 channels at high levels, similar V5-JPH2 cluster signals were shown. For example, expression of V5-FL-JPH2 led to cluster signals closely associated with RyR1 clusters. In contrast, the V5-ΔTM-JPH2 signal pattern showed no systematic spatial relations with the RyR1 cluster signals but a rather continuous reticular distribution, principally similar to the NRCM data.

Third, expression of V5-JPH2 proteins in immature C2C12 myoblasts, expressing very low levels of endogenous RyR (not detected by IF imaging), resulted in significant differences between V5-FL-JPH2 and V5-ΔTM-JPH2 signal distribution indicating distinct intracellular clustering and homomeric-organisation behaviours. The quantitative analysis revealed that V5-FL-JPH2 signals were likely to form clusters in sheet-like domains of the ER/SR,

whereas V5-ΔTM-JPH2 signals were ubiquitously distributed throughout the ER/SR apparent by an uninterrupted reticular signal distribution.

In summary, N-terminal truncation of all cytosolic JPH2 domains diminished cluster formation and spatial association with RyR clusters in situ. This suggests that the cytosolic divergent region and/or the α-helical domain and/or the MORN motifs might play an important role for JPH2 clustering and subcellular self-organisation in the ER/SR membrane organelle.

5.2 STED nanoscopy for JPH2 cluster analysis

Recently, STED nanoscopy was successfully applied to visualise subcellular structures in cardiomyocytes (Wagner et al. 2012; Wagner et al. 2014; Brandenburg et al. 2016). Thus, by combining STED nanoscopy with photostable STED dyes it is possible to resolve signals beyond the diffraction barrier even in large muscle cells, i.e. up to ~60 nm resolution (Kohl et al. 2013). In contrast, diffraction-limited confocal microscopy methods provide a resolution of ~250 nm (Kohl et al. 2013). A STED superresolution study resolved TT cross-sections deep in living cardiomyocytes quantified as ~200 nm average diameter, whereas confocal imaging provided mainly larger dimensions based on blurred signals (Wagner et al. 2012). Consequently, diffraction limited microscopy methods are not suitable for the quantitative analysis of structural details beyond the diffraction barrier. By using STED nanoscopy, it is possible to distinguish structural details in subcellular structures, e.g. JPH2 and RyR2 clusters and judge their nanoscale arrangement (Figure 26).

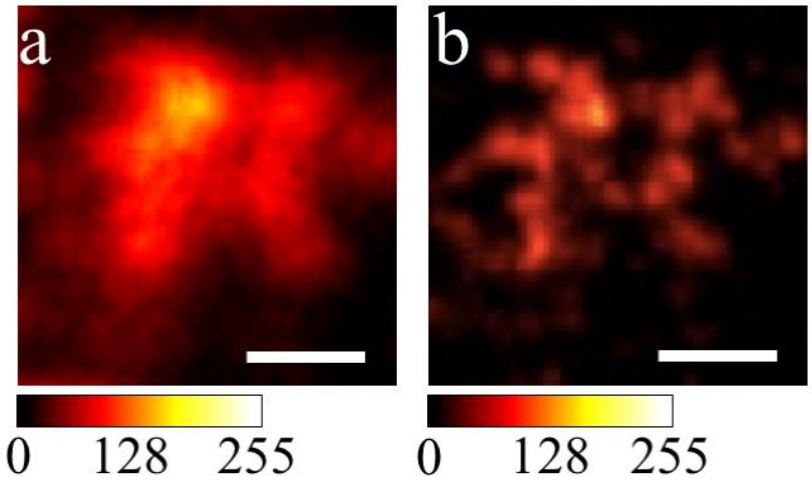

Figure 26: Comparison between confocal and STED imaging

Conventional microscopy techniques are limited in resolution by light diffraction. STED nanoscopy provided the possibility to visualise signal patterns at a nanometric scale. **(a)**: Diffraction limited confocal image of V5-FL-JPH2 in a C2C12 myoblast at a resolution of ~250 nm. **(b)**: The same V5-FL-JPH2 structure at a resolution of ~60 nm in C2C12 myoblast using the same imaging system with the STED laser switched on. The lookup table indicates the brightness rank of signals. Scale bars: 200 nm. V5-FL-JPH2 signals were detected by mouse anti-V5 antibody and anti-mouse AlexaFluor 568. For detailed information about antibody dilution, please refer to Materials and Methods (2.1.4 and 2.1.5).

5.3 Effect of JPH2 knockout and overexpression

JPH2 is known to play a key role for maintaining the structure of CRUs. Takeshima et al. have shown that JPH2 knockout in mice is embryonic lethal (Takeshima et al. 2000). Furthermore, JPH2 knockdown through shRNA expression in adult mice led to a decreased number of CRUs and highly irregular junctional widths (van Oort et al. 2011). Moreover, it was shown that JPH2 knockdown results in an increased diastolic Ca^{2+} leak through RyR2 channels (Beavers et al. 2013).

In contrast, JPH2 overexpression in mice was shown to stabilise TTs in cardiac cells from hearts that faced LV pressure overload (Guo et al. 2014). As an effect of the overexpression the authors identified an increased jSR/TT contact length that resulted in a small fraction of convoluted TTs (Guo et al. 2014). Interestingly, this structural change did not affect the contractile function of murine heart muscle cells but attenuated the development of HF (Guo et al. 2014). This result is in line with a study of Munro et al. who showed that JPH2 overexpression in mice leads to an increased colocalisation of JPH2 and RyR2 (Munro et al.

2016). Thus, a high expression level of JPH2 might be useful as intervention to prevent TT remodeling due to cardiac stress.

The results of this thesis show that the expression of recombinant full length JPH2 in C2C12 and NRCM cells led to clustered structures with a distinct ER/SR organisation. Furthermore, there was a clear colocalisation between recombinant JPH2 and endogenous RyR1 and RyR2 channels. In C2C12 and NRCM cells, clusters of recombinant JPH2 and their association with RyR2 clusters were very similar to endogenous JPH2.

5.4 JPH2 signal pattern

The specific signal pattern of expressed V5-FL-JPH2 indicated both maturation and cell type dependent differences between signal clusters. Typical V5-FL-JPH2 clusters were visualised in undifferentiated C2C12 myoblasts and differentiated myotubes (day 7) as well as NRCM cells. Accordingly, V5-FL-JPH2 clusters were present in cells with low levels of endogenous JPH2 and RyR1 (i.e. C2C12 myoblasts) as well as high levels of endogenous JPH2 and RyR1 (i.e. differentiated C2C12 myotubes). On average, the detected cluster diameter amounted to 150 ± 30 nm. Furthermore, in C2C12 myotubes and NRCM cells with high levels of endogenous RyR2, the clustered signals of recombinant JPH2 and RyR channels were spatially associated. Finally, expression of truncated V5-ΔDR-TM-JPH2 in NRCM cells led to similar results compared to V5-FL-JPH2.

Ziman et al. have shown a spatial relation between endogenous RyR2 and JPH2 in rat cardiomyocytes (Ziman et al. 2010). Using superresolution dSTORM microscopy Jayasinghe et al. resolved the arrangement of JPH2 and RyR2 signals in clusters (Jayasinghe et al. 2012). Similar to our data they showed that the endogenous JPH2 and RyR2 signals are spatially significantly associated (Jayasinghe et al. 2012). Furthermore, it was described that JPH2 signals are not constrained to specific positions inside clusters but rather interspersed throughout the RyR2 cluster area (Jayasinghe et al. 2012).

In conclusion, our data extends recent studies in terms of JPH2 organisation in clusters. Especially, the influence of specific JPH2 domains on homomeric formation has not been investigated in detail so far.

5.5 JPH2 cluster analysis

The spatial relation between recombinant JPH2 and endogenous RyR2 is complex. The V5-FL-JPH2 clusters were variable in size and shape (~150 nm). This is consistent with Baddeley et al., who reported on RyR2 clusters with elongated shapes of variable size (mean 107 nm in diameter) (Baddeley et al. 2009). In addition, Munro et al. investigated the RyR2 cluster shape and the colocalisation between endogenous JPH2 and RyR2 in JPH2 knockdown mice as well as cardiac specific JPH2 overexpressing mice by using single particle detection dSTORM microscopy (Munro et al. 2016). In comparison to wild-type mice, JPH2 knockdown led to a reduced colocalisation between RyR2 and JPH2 while the JPH2 cluster size was unchanged (Munro et al. 2016). In contrast, JPH2 overexpression resulted in significantly increased colocalisation between RyR2 and JPH2 as well as an increased mean JPH2 cluster size (Munro et al. 2016).

Taken together, the expression of recombinant V5-FL-JPH2 led to signal clusters that were variable in size and shape and in close spatial proximity to RyR2 clusters, similar to endogenous JPH2.

5.6 Effect of JPH2 domain truncations on the spatial association with RyR2

N-terminal truncations of JPH2 led to an altered ER/SR localisation and impaired the specific spatial association with endogenous RyR2 channels in clusters. Expression of V5-ΔTM-JPH2 resulted in an ubiquitous reticular yet not a clustered signal distribution. In contrast, both V5-FL-JPH2 and V5-ΔDR-TM-JPH2 expression resulted in the formation of clusters in NRCM cells.

Earlier studies showed an interaction of JPH2 with different members of CRUs (van Oort et al. 2011; Beavers et al. 2013). It was shown that JPH2 stabilises RyR2 channels and that JPH2 knockdown leads to an increased Ca^{2+} leak through RyR2 (Beavers et al. 2013).

Furthermore, Beavers et al. revealed that the interaction between JPH2 and RyR2 is mediated by the cytosolic joining region of JPH2 (Beavers et al. 2013). In this context, the E169K mutation in the joining region of JPH2 was associated with HCM and was found to decrease the binding of JPH2 and RyR2 (Beavers et al. 2013). In addition, the C-terminal TM domain

and divergent region of JPH2 were suggested to play a role for the association between JPH2 and RyR2 (Landstrom et al. 2014).

In summary, the described signal pattern of V5-ΔDR-TM-JPH2 (includes the divergent region and the TM domain while α-helix and MORN-motifs were deleted) indicates that the divergent region may mediate the association with RyR2 channels. This finding is consistent with the hypothesis of Garbino et al. who suggested that the divergent region of JPHs might mediate isoform-specific association with specific binding partners within CRUs (Garbino et al. 2009).

5.7 Distinct ER/SR distribution of recombinant JPH2

Expression of V5-full-length (FL)-JPH2 resulted in clustered structures with distinct ER/SR distributions. This signal distribution was both in cells with high (i.e. differentiated C2C12 myotubes) and low expression (i.e. undifferentiated C2C12 myoblasts) rates of endogenous RyR1 channels (Figure 27). In contrast, expression of truncated V5-ΔTM-JPH2 resulted in a global signal distribution throughout the ER/SR-network with a pan-reticular appearance. Interestingly, Baddeley et al. speculated that RyR cluster formation might be mediated by JPH2 which functions as a "seed-site" in this process (Baddeley et al. 2009; Jayasinghe et al. 2012). In contrast, Ziman et al. who investigated the maturation of the TT membrane system in rat cardiomyocytes, concluded that JPH2 clustering depends on prior localisation of RyR2 in close proximity to Z-discs (Ziman et al. 2010).

In conclusion, full-length JPH2 expression induced clustered structures in C2C12 myoblasts, which have low endogenous levels of RyR1. This indicates that JPH2 homooligomerisation can be induced by increased protein expression and in the absence of detectable RyR1 channel clusters.

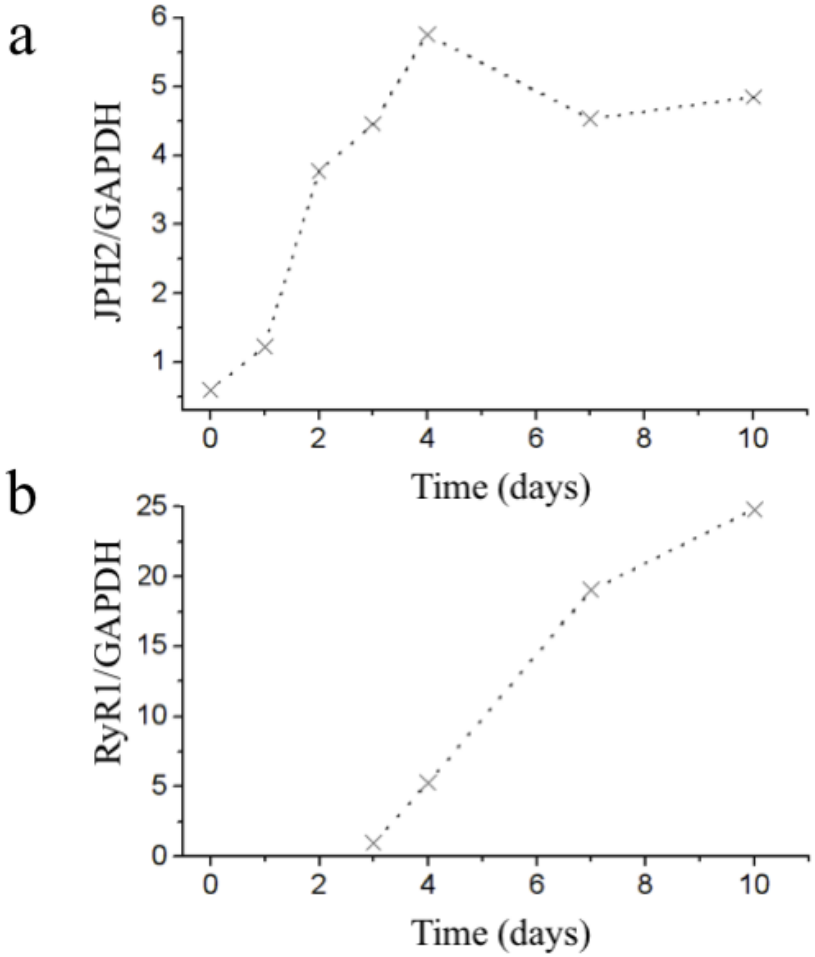

Figure 27: JPH2 and RyR1 expression level in C2C12 cells during maturation

The expression of endogenous JPH2 and RyR1 increases during C2C12 cell maturation. C2C12 myoblasts were differentiated by high cell confluency and serum depletion (see Materials and Methods, 2.2.1.3). **(a)**: Western blot analysis has shown an increase of JPH2 expression after 1 day of incubation and plasmid transfection. **(b)**: In contrast, RyR1 expression was measurable after 3-4 days of incubation. Glyceraldehyde-3-phosphate dehydrogenase (GAPDH) served as a loading control. The western blot data was kindly provided by Dr. G Weninger (Unpublished data; Dr. G. Weninger, AG Lehnart, Heart Research Center Göttingen).

5.8 Factors stabilising JPH2 retention in the ER/SR

In eukaryotic cells, certain newly synthesised proteins can enter the a secretory pathway (Rothman and Orci 1992). They enter the ER and then move to the Golgi apparatus where they are modified (Rothman and Orci 1992). Other proteins, e.g. glucose-regulated proteins grp78 and grp94, reside in the ER/SR to maintain its structural and functional integrity (Pelham 1986). This ER/SR residency is mediated by distinct sequences, such as C-terminal KDEL (Munro and Pelham 1987). This is mainly achieved in two different ways: a) a

missing ER/SR exit signal (static retention) or b) a dynamic retrieval of escaped proteins through distinct sequences (e.g. KDEL) (Teasdale and Jackson 1996).

The stabilisation mechanism of JPH2 in the ER/SR has not been established. Other tail-anchored proteins such as cytochrome b5 are recycled between the ER and the Golgi apparatus (Pedrazzini et al. 2000). Therefore, distinct JPH2 mutants (His6-ΔTM-JPH2-C678A, His6-ΔTM-JPH2-N684L, His6-ΔTM-JPH2-C678A-N684L, His6-FL-JPH2-4L, His6-FL-JPH2-8L) were used to investigate how JPH2 is retained in the ER/SR. Our data has shown that these mutations did not cause a significant redistribution of JPH2 signals, i.e. to the cell periphery. Either the mutations were not sufficient to disturb retrieval of JPH2 or JPH2 is retained in the ER/SR by static retention. Furthermore, a possible colocalisation between the JPH2 mutants and the ER-Golgi intermediate compartment (ERGIC) was investigated. However, the visualised gap arrangement between the JPH2 and ERGIC signals is not consistent with a JPH2 retrieval mechanism between the ER/SR and the Golgi apparatus.

In conclusion, distinct C-term mutation of JPH2 did not disturb JPH2 retrieval. Thus, JPH2 may be retained in the ER/SR by static retention.

5.9 JPH1 and JPH2 in cardiac and skeletal muscle cells

JPH1 is predominantly expressed in skeletal muscle cells, whereas JPH2 is distributed in both skeletal and cardiac muscle cells (Takeshima et al. 2000). It has been reported that JPH1 and JPH2 interact with Cav1.1, RyR1 and Cav3 in C2C12 myotubes (Golini et al. 2011). Although JPH1 and JPH2 are members of the same protein family, there might be important differences in protein interactions, e.g. with RyR1 (Phimister et al. 2007). JPH2 is spatially associated with RyR1 in skeletal muscle cells, whereas JPH1 directly binds RyR1 via C-terminal thiol groups (Phimister et al. 2007; Golini et al. 2011).

In extension to these earlier studies, our data indicate a homooligomerisation of recombinant JPH2 in C2C12 and NRCM cells. This raises the question of a potential direct JPH2/JPH2 or JPH1/JPH2 interaction that has not been investigated so far. In this context, our results create a molecular cell biology basis for future investigation of protein interactions by proximity proteomics, i.e. through APEX-JPH2 fusion proteins expressed in cells.

5.10 Conclusion and Outlook

Taken together, the present data provide insight into clustering and self-organisation of recombinantly expressed JPH2 in different cell types. By using superresolution STED microscopy it was possible to resolve details about JPH2 clustering. The hypothesis that N-terminal truncation variants of JPH2 lead to an altered ER/SR distribution and clustering behaviour was verified. The finding that full-length JPH2 as well as V5-ΔDR-TM-JPH2 (includes the divergent region and the TM domain while α-helix and MORN-motifs were deleted) are able to form clusters that are spatially associated with RyR2 signals emphasises the important role of the divergent region concerning JPH2 organisation. Since the loss of CRU integrity is a proposed mechanism in the pathogenesis of heart failure, this finding may be relevant for JPH2 redistribution and TT remodeling.

This thesis creates a basis for future projects to investigate advanced proteomic interaction questions. In addition, it might be interesting to use intracellular Ca^{2+} imaging in cells that express the recombinant JPH2 constructs. Furthermore, JPH2 self-organisation in cells with low RyR1 expression (i.e. immature C2C12 myoblasts) can be exploited to identify unknown interaction partners that may be relevant concerning JPH2 clustering and ER/SR distribution. Finally, the investigation of the basic molecular JPH2/JPH2 self-interaction can be motivated by this thesis work.

6. Abstract

Junctophilin-2 (JPH2) –a tail-anchored protein located in the sarcoplasmic reticulum (SR) membrane– is known to stabilise Calcium Release Units (CRUs) in the ~12 nm wide junction between the sarcolemma (SL) and the SR. Recently, a decreased expression of the JPH2 protein was associated with a disruption of CRU function and distinct ultrastructural changes in cardiac dilation and hypertrophy. While an essential role of JPH2 for CRU stabilisation has emerged as a principle mechanism of junctional SR membrane contacts, the mechanisms behind JPH2 clustering and its organisation remain unknown. In this research work, I have studied the signal distribution based on recombinant JPH2 expression constructs in the endoplasmic or sarcoplasmic reticulum (ER/SR) in different cell models in order to investigate the subcellular mechanisms of JPH2 clustering.

Expression of different JPH2 truncation constructs was studied in HEK293a cells, C2C12 myoblasts, C2C12 myotubes and neonatal rat cardiomyocytes (NRCM) using STimulated Emission Depletion (STED) superresolution microscopy and quantitative image analysis. N-terminal truncation of all cytosolic JPH2 domains resulted in a loss of local JPH2 clustering and pan-ER/SR distribution.

Our data show a JPH2 construct-specific and cell type-dependent clustering behaviour. Specifically, the expression of recombinant full-length JPH2 and N-terminally truncated JPH2 (the latter including the divergent region and the TM domain while the α-helix and the MORN-motifs were deleted) led to a clustered signal pattern that was spatially associated with Ryanodine Receptor type 2 (RyR2) channels in NRCMs. In contrast, the signal distribution of truncated JPH2 devoid of all cytosolic domains resulted in a pan-ER/SR distribution and altered spatial relations with RyR2 channels. In conclusion, the divergent region of JPH2 may promote at least in part the subcellular formation of JPH2 self-clustering and its local stabilisation in ER/SR nanodomains.

7. List of references

Abbe E (1873): Beiträge zur Theorie des Mikroskops und der mikroskopischen Wahrnehmung. Arch Mikrosk Anat 9, 413–418

Baddeley D, Jayasinghe ID, Lam L, Rossberger S, Cannell MB, Soeller C (2009): Optical single-channel resolution imaging of the ryanodine receptor distribution in rat cardiac myocytes. Proc Natl Acad Sci U S A 106, 22275–22280

Beavers DL, Wang W, Ather S, Voigt N, Garbino A, Dixit SS, Landstrom AP, Li N, Wang Q, Olivotto I, et al. (2013): Mutation E169K in junctophilin-2 causes atrial fibrillation due to impaired RyR2 stabilization. J Am Coll Cardiol 62, 2010–2019

Beavers DL, Landstrom AP, Chiang DY, Wehrens XHT (2014): Emerging roles of junctophilin-2 in the heart and implications for cardiac diseases. Cardiovasc Res 103, 198–205

Bennett HJ, Davenport JB, Collins RF, Trafford AW, Pinali C, Kitmitto A (2013): Human junctophilin-2 undergoes a structural rearrangement upon binding PtdIns(3,4,5)P3 and the S101R mutation identified in hypertrophic cardiomyopathy obviates this response. Biochem J 456, 205–217

Bers DM (2002): Cardiac excitation-contraction coupling. Nature 415, 198–205

Bers DM, Stiffel VM (1993): Ratio of ryanodine to dihydropyridine receptors in cardiac and skeletal muscle and implications for E-C coupling. Am J Physiol 264, 1587–1593

Born M, Wolf E (Hrsg.): Principles of optics - Electromagnetic theory of propagation, interference and diffraction of light. 7th edition; Cambridge University Press, Cambridge 2002

Brandenburg S, Kohl T, Williams GS, Gusev K, Wagner E, Rog-Zielinska EA, Hebisch E, Dura M, Didié M, Gotthardt M, et al. (2016): Axial tubule junctions control rapid calcium signaling in atria. J Clin Invest 126, 3999–4015

Collins JH, Potter JD, Horn MJ, Wilshire G, Jackman N (1973): The amino acid sequence of rabbit skeletal muscle troponin C: Gene replication and homology with calcium-binding proteins from carp and hake muscle. FEBS Lett 36, 268–272

Ebashi S, Kodama A (1965): A new protein factor promoting aggregation of tropomyosin. J Biochem 58, 107–108

Fabiato A (1983): Calcium-induced release of calcium from the cardiac sarcoplasmic reticulum. Am J Physiol 245, 1–14

Fabiato A, Fabiato F (1978): Calcium-induced release of calcium from the sarcoplasmic reticulum of skinned cells from adult human, dog, cat, rabbit, rat and frog hearts and from fetal and new-born rat ventricles. Ann N Y Acad Sci 307, 491–522

Franzini-Armstrong C, Protasi F, Ramesh V (1999): Shape, size, and distribution of Ca(2+) release units and couplons in skeletal and cardiac muscles. Biophys J 77, 1528–1539

Fritschy J-M, Härtig W: Immunofluorescence. In: eLS. doi: 10.1038/npg.els.0001174

Galbiati F, Engelman JA, Volonte D, Zhang XL, Minetti C, Li M, Hou H, Kneitz B, Edelmann W, Lisanti MP (2001): Caveolin-3 null mice show a loss of caveolae, changes in the microdomain distribution of the dystrophin-glycoprotein complex, and t-tubule abnormalities. J Biol Chem 276, 21425–21433

Garbino A, van Oort RJ, Dixit SS, Landstrom AP, Ackerman MJ, Wehrens XHT (2009): Molecular evolution of the junctophilin gene family. Physiol Genomics 37, 175–186

Golini L, Chouabe C, Berthier C, Cusimano V, Fornaro M, Bonvallet R, Formoso L, Giacomello E, Jacquemond V, Sorrentino V (2011): Junctophilin 1 and 2 proteins interact with the L-type Ca2+ channel dihydropyridine receptors (DHPRs) in skeletal muscle. J Biol Chem 286, 43717–43725

Grotjohann T, Testa I, Reuss M, Brakemann T, Eggeling C, Hell SW, Jakobs S (2012): rsEGFP2 enables fast RESOLFT nanoscopy of living cells. eLife 1, e00248

Gwathmey JK, Copelas L, MacKinnon R, Schoen FJ, Feldman MD, Grossman W, Morgan JP (1987): Abnormal intracellular calcium handling in myocardium from patients with end-stage heart failure. Circ Res 61, 70–76

Gwathmey JK, Slawsky MT, Hajjar RJ, Briggs GM, Morgan JP (1990): Role of intracellular calcium handling in force-interval relationships of human ventricular myocardium. J Clin Invest 85, 1599–1613

Guo A, Zhang X, Iyer VR, Chen B, Zhang C, Kutschke WJ, Weiss RM, Franzi-Armstrong C, Song LS (2014): Overexpression of junctophilin-2 does not enhance baseline function but attenuates heart failure development after cardiac stress. Proc Natl Acad Sci U S A 111, 12240–12245

Guo A, Hall D, Zhang C, Peng T, Miller JD, Kutschke W, Grueter CE, Johnson FL, Lin RZ, Song LS (2015): Molecular Determinants of Calpain-dependent Cleavage of Junctophilin-2 Protein in Cardiomyocytes. J Biol Chem 290, 17946–17955

Hasenfuß G (2014): Herzinsuffizienz. Eine medizinische Herausforderung. Internist 55, 645–646

Hasenfuß G, Mulieri LA, Leavitt BJ, Allen PD, Haeberle JR, Alpert NR (1992): Alteration of contractile function and excitation-contraction coupling in dilated cardiomyopathy. Circ Res 70, 1225–1232

Hasenfuß G, Schillinger W, Lehnart SE, Preuss M, Pieske B, Maier LS, Prestle J, Minami K, Just H (1999): Relationship between Na+-Ca2+-exchanger protein levels and diastolic function of failing human myocardium. Circulation 99, 641–648

Hayashi T, Martone ME, Yu Z, Thor A, Doi M, Holst MJ, Ellisman MH, Hoshijima M (2009): Three-dimensional electron microscopy reveals new details of membrane systems for Ca2+ signaling in the heart. J Cell Sci 122, 1005–1013

Hebisch E, Wagner E, Westphal V, Sieber JJ, Lehnart SE (2017): A protocol for registration and correction of multicolour STED superresolution images. J Microsc 267, 160-175

Hell SW, Wichmann J (1994): Breaking the diffraction resolution limit by stimulated emission: stimulated-emission-depletion fluorescence microscopy. Opt Lett 19, 780–782

Ideker RE, Kong W, Pogwizd S (2009): Purkinje Fibers and Arrythmias. Pacing Clin Electrophysiol 32, 283–285

Inui M, Saito A, Fleischer S (1987): Purification of the ryanodine receptor and identity with feet structures of junctional terminal cisternae of sarcoplamic reticulum from fast skeletal muscle. J Biol Chem 262, 1740–1747

Ito K, Komazaki S, Sasamoto K, Yoshida M, Nishi M, Kitamura K, Takeshima H (2001): Deficiency of triad junction and contraction in mutant skeletal muscle lacking junctophilin

type 1. J Cell Biol 154, 1059–1067

Jayasinghe ID, Baddeley D, Kong CHT, Wehrens XHT, Cannell MB, Soeller C (2012): Nanoscale organization of junctophilin-2 and ryanodine receptors within peripheral couplings of rat ventricular cardiomyocytes. Biophys J 102, 19–21

Jayasinghe ID, Clowsley AH, Lin R, Lutz T, Harrison C, Green E, Baddeley D, Di Michele L, Soeller C (2018): True Molecular Scale Visualization of Variable Clustering Properties of Ryanodine Receptors. Cell Reports 22, 557–567

Jugdutt BI (2003): Ventricular remodeling after infarction and the extracellular collagen matrix: when is enough enough? Circulation 108, 1395–1403

Kaether C, Scheuermann J, Fassler M, Zilow S, Shirotani K, Valkova C, Novak B, Kacmar S, Steiner H, Haass C (2007): Endoplasmic reticulum retention of the γ-secretase complex component Pen2 by Rer1. EMBO Rep 8, 743–748

Kohl T, Westphal V, Hell SW, Lehnart SE (2013): Superresolution microscopy in heart - cardiac nanoscopy. J Mol Cell Cardiol 58, 13–21

Landstrom AP, Kellen CA, Dixit SS, van Oort RJ, Garbino A, Weisleder N, Ma J, Wehrens XHT, Ackerman MJ (2011): Junctophilin-2 expression silencing causes cardiocyte hypertrophy and abnormal intracellular calcium-handling. Circ Heart Fail 4, 214–223

Landstrom AP, Beavers DL, Wehrens XHT (2014): The junctophilin family of proteins: From bench to bedside. Trends Mol Med 20, 353–362

Lawson MA, Purslow PP (2000): Differentiation of myoblasts in serum-free media: effects of modified media are cell line-specific. Cells Tissues Organs 167, 130–137

Li H, Ding X, Lopez JR, Takeshima H, Ma J, Allen PD, Eltit JM (2010): Impaired Orai1-mediated resting Ca2+ entry reduces the cytosolic [Ca2+] and sarcoplasmic reticulum Ca2+ loading in quiescent junctophilin 1 knock-out myotubes. J Biol Chem 285, 39171–39179

Minamisawa S, Oshikawa J, Takeshima H, Hoshijima M, Wang Y, Chien KR, Ishikawa Y, Matsuoka R (2004): Junctophilin type 2 is associated with caveolin-3 and is down-regulated in the hypertrophic and dilated cardiomyopathies. Biochem Biophys Res Commun 325, 852–856

Munro ML, Jayasinghe ID, Wang Q, Quick A, Baddeley D, Wehrens XHT, Soeller C (2016): Junctophilin-2 in the nanoscale organisation and functional signalling of ryanodine receptor clusters in cardiomyocytes. J Cell Sci 129, 4388–4398

Munro S, Pelham HR (1987): A C-terminal signal prevents secretion of luminal ER proteins. Cell 48, 899–907

Murphy RM, Dutka TL, Horvath D, Bell JR, Delbridge LM, Lamb GD (2013): Ca2+-dependent proteolysis of junctophilin-1 and junctophilin-2 in skeletal and cardiac muscle. J Physiol 591, 719–729

Nishi M, Sakagami H, Komazaki S, Kondo H, Takeshima H (2003): Coexpression of junctophilin type 3 and type 4 in brain. Brain Res Mol Brain Res 118, 102–110

Pelham HR (1986): Speculations on the functions of major heat shock and glucose-related proteins. Cell 46, 959-961

Phimister AJ, Lango J, Lee EH, Ernst-Russell MA, Takeshima H, Ma J, Allen PD, Pessah IN (2007): Conformation-dependent stability of junctophilin 1 (JP1) and ryanodine receptor type 1 (RyR1) channel complex is mediated by their hyper-reactive thiols. J Biol Chem 282, 8667–8677

Prosser BL, Ward CW, Lederer WJ (2010): Subcellular Ca2+ signaling in the heart: the role of the ryanodine receptor sensitivity. J Gen Phyiol 136, 135–142

Quick AP, Landstrom AP, Wang Q, Beavers DL, Reynolds JO, Barreto-Torres G, Tran V, Showell J, Philippen LE, Morris SA, et al. (2017): Novel Junctophilin-2 Mutation A405S Is Associated With Basal Septal Hypertrophy and Diastolic Dysfunction. JACC Basic Transl Sci 2, 56–67

Reynolds JO, Chiang DY, Wang W, Beavers DL, Dixit SS, Skapura DG, Landstrom AP, Song L-S, Ackerman MJ, Wehrens XHT (2013): Junctophilin-2 is necessary for T-tubule maturation during mouse heart development. Cardiovasc Res 100, 44–53

Rhee H-W, Zou P, Udeshi ND, Martell JD, Mootha VK, Carr SA, Ting AY (2013): Proteomic Mapping of Mitochondria in Living Cells via Spatially-Restricted Enzymatic Tagging. Science 339, 1328–1331

Rothman JE, Orci L (1992): Molecular dissection of the secretory pathway. Nature 355,

409–415

Sandow A (1952): Excitation-contraction coupling in muscular response. Yale J Biol Med 25, 176–201

Schneider MF, Chandler WK (1973): Voltage dependent charge movement of skeletal muscle: a possible step in excitation-contraction coupling. Nature 242, 244–246

Song L-S, Sobie EA, McCulle S, Lederer WJ, Balke CW, Cheng H (2006): Orphaned ryanodine receptors in the failing heart. Proc Natl Acad Sci U S A 103, 4305–4310

Stern MD (1992): Theory of excitation-contraction coupling in cardiac muscle. Biophys J 63, 497–517

Sun XH, Protasi F, Takahashi M, Takeshima H, Ferguson DG, Franzini-Armstrong C (1995): Molecular architecture of membranes involved in excitation-contraction coupling of cardiac muscle. J Cell Biol 129, 659–671

Takeshima H, Komazaki S, Nishi M, Iino M, Kangawa K (2000): Junctophilins: a novel family of junctional membrane complex proteins. Mol Cell 6, 11–22

Teasdale RD, Jackson MR (1996): Signal-mediated sorting of membrane proteins between the endoplasmic reticulum and the golgi apparatus. Annu Rev Cell Dev Biol 12, 27–54

van Oort RJ, Garbino A, Wang W, Dixit SS, Landstrom AP, Gaur N, De Almeida AC, Skapura DG, Rudy Y, Burns AR, et al. (2011): Disrupted junctional membrane complexes and hyperactive ryanodine receptors after acute junctophilin knockdown in mice. Circulation 123, 979–988

Wagner E, Lauterbach MA, Kohl T, Westphal V, Williams GSB, Steinbrecher JH, Streich J-H, Korff B, Tuan H-TM, Hagen B, et al. (2012): Stimulated emission depletion live-cell super-resolution imaging shows proliferative remodeling of T-tubule membrane structures after myocardial infarction. Circ Res 111, 402–414

Wagner E, Brandenburg S, Kohl T, Lehnart SE (2014): Analysis of tubular membrane networks in cardiac myocytes from atria and ventricles. J Vis Exp 92, 1–19

Woo JS, Kim DH, Allen PD, Lee EH (2008): TRPC3-interacting triadic proteins in skeletal muscle. Biochem J 411, 399–405

Woo JS, Hwang J-H, Ko J-K, Kim DH, Ma J, Lee EH (2009): Glutamate at position 227 of junctophilin-2 is involved in binding to TRPC3. Mol Cell Biochem 328, 25–32

Wu C-YC, Jia Z, Wang W, Ballou LM, Jiang Y-P, Chen B, Mathias RT, Cohen IS, Song L-S, Entcheva E, et al. (2011): PI3Ks maintain the structural integrity of T-tubules in cardiac myocytes. PloS One 6, e24404

Xu M, Wu HD, Li RC, Zhang HB, Wang M, Tao J, Feng XH, Guo YB, Li SF, Lai ST, et al. (2012): Mir-24 regulates junctophilin-2 expression in cardiomyocytes. Circ Res 111, 837–841

Yancy CW, Jessup M, Bozkurt B, Butler J, Casey Jr. DE, Drazner MH, Fonarow GC, Geraci SA, Horwich T, Januzzi JL, et al. (2013): 2013 ACCF/AHA Guideline for the Management of Heart Failure: A Report of the American College of Cardiology Foundation/American Heart Association Task Force on Practice Guidelines. J Am Coll Cardiol 62, 147–239

Zhang HB, LI RC, Xu M, Xu SM, Lai YS, Wu HD, Xie XJ, Gao W, Ye H, Zhang YY, Meng X, Wang SQ (2013): Ultrastructural uncoupling between T-tubules and sarcoplasmic reticulum in human heart failure. Circ Res 98, 269–276

Ziman AP, Gómez-Viquez NL, Bloch RJ, Lederer WJ (2010): Excitation-contraction coupling changes during postnatal cardiac development. J Mol Cell Cardiol 48, 379–386

Poster contributions

Lehnart SE (2016): Local molecular nanodomain regulation of cardiac ryanodine receptor function. On-site visit SFB1190 “Compartmental Gates and Contact Sites in Cells” in Göttingen.

Zandt M, Lehnart SE (2017): Domain-dependent clustering and targeting mechanisms of Junctophilin-2 in the endo-/sarcoplasmic reticulum in human kidney, cardiac and skeletal muscle cells. On-site visit IRTG1816 in Göttingen.

Danksagung

Der größte Dank gilt meinem Doktorvater, Herrn Prof. Dr. Stephan E. Lehnart, für seine stetige Unterstützung und motivierende sowie freundliche Art. Die vielen Hinweise, Anregungen sowie die geduldige Beantwortung aller meiner Fragen verhalfen mir zur erfolgreichen Durchführung der Experimente sowie zur Verschriftlichung meiner Doktorarbeit. Des Weiteren unterstützte mich Herr Prof. Lehnart im Bewerbungsprozess für ein Promotionsstipendium der International Research Training Group 1816. Ich hatte mit Hilfe der Unterstützung von Herrn Prof. Dr. Lehnart die Möglichkeit, meine Daten führenden Wissenschaftlern wie Prof. Dr. Karl-Heinz Kuck (ehemaliger DGK-Präsident) oder Prof. Dr. Stefan W. Hell (Nobelpreis für Chemie 2014) vorzustellen. Zuletzt bedanke ich mich sehr herzlich für die Korrektur dieser Doktorarbeit.

Ganz besonders bedanke ich mich bei meinen wissenschaftlichen Betreuern Herrn Dr. Tobias Kohl und Herrn Dr. Gunnar Weninger, welche mich tatkräftig bei der Durchführung der Experimente sowie der Auswertung der Ergebnisse unterstützten. Während der letzten drei Jahre konnte ich mich immer auf Herrn Dr. Kohl und Herrn Dr. Weninger verlassen, ohne deren kompetenten und zuverlässigen Beitrag die Vollendung dieser Doktorarbeit nicht möglich gewesen wäre. Besonders bedanke ich mich für den menschlichen und freundlichen Umgang.

Des Weiteren bedanke ich mich herzlich bei Frau Birgit Schumann, welche mich tatkräftig bei der praktischen Arbeit im Labor unterstützte. Ohne die praktische Erfahrung und die zahlreichen Hinweise von Frau Schumann wäre die zügige Entwicklung vieler Protokolle nicht möglich gewesen. Ich danke auch ihr für den tollen Umgang und die freundliche Art.

Schließlich möchte ich mich ganz herzlich beim Herzzentrum der Universitätsmedizin Göttingen sowie der International Research Training Group für die Realisierung und Finanzierung meiner Doktorarbeit bedanken. Die wöchentlichen Seminare und Methodenkurse haben mir sehr viel Spaß gemacht und mein theoretisches Know-how auf dem Gebiet der Herz-Kreislaufforschung gefördert.